Author Summary

iPSCs change to resemble ESCs via two phases: the transgene-dependent phase, in which the transcription factors act to transform somatic cells into pluripotent stem cells, and the transgene-independent phase, in which the transcription factors are silenced. In this study, we established human iPSCs derived from 5 different cell types by retroviral infection of the Yamanaka 4 factors, and we identified 8 novel epigenetic markers (*SALL4*, *EPHA1*, *PTPN6*, *RAB25*, *GBP4*, *LYST*, *SP100*, and *UBE1L*) by comprehensive DNA methylation analysis. The aberrant hyper-methylation in iPSCs occurred stochastically throughout the genome and decreased during the long-term iPSC reprogramming, suggesting that the aberrant stochastic hyper-methylation and their convergence are a direct cause of the transgene-independent phase of iPS reprogramming. These results favor the stochastic model of the Yamanaka model rather than the elite model. In addition, the stem cell–specific methylation states and the epigenetic difference between iPSCs and ESCs are useful indices for evaluating human iPSCs in therapeutic applications.

(*OCT-3/4*, *SOX2*, *c-MYC*, and *KLF4*) (Figure 1A, 1B and Table S1). These cells clearly showed human ES-like characters in terms of morphology; cell-surface antigens; gene expression of stem cell markers; teratoma formation in which these cells differentiated to various tissues including neural tissues (ectoderm), cartilage (mesoderm), and epithelial tissues (endoderm); growth (more than 20 passages); and DNA methylation patterns at *OCT-3/4* and *NANOG* promoter regions (Figures S1, S2, S3). Short tandem repeat (STR) analysis showed clonality between the respective iPSC lines and their parent cells (Table S2). Silencing of transgenes and normal karyotypes of iPSCs were also confirmed (Figure S4 and Table S3).

Analysis of DNA methylation profiles

To investigate the dynamics of DNA methylation in pluripotent stem cells, we examined 5 ESC lines (HUESCs) [23,24], 22 iPSC lines, their parent cells and 201B7, using Illumina's Infinium HumanMethylation27 BeadChip. In total, 24,273 CpG sites in 13,728 genes were analyzed, along with 33 human cell lines (Table S1). The iPSC line "201B7" was generated from human skin fibroblasts [8]. Quantitative scores of DNA methylation levels were obtained as β-values determined from the Illumina analysis, ranging from "0", for completely unmethylated, to "1", for completely methylated. We also performed genome-wide gene expression analysis using the Agilent Whole Human Genome Microarray chips. As assessed by unsupervised hierarchical clustering analysis and scatter plot of DNA methylation and gene expression data, human iPSCs could be clearly discriminated from their parent cells and were similar to ESCs (Figure 1C and Figure

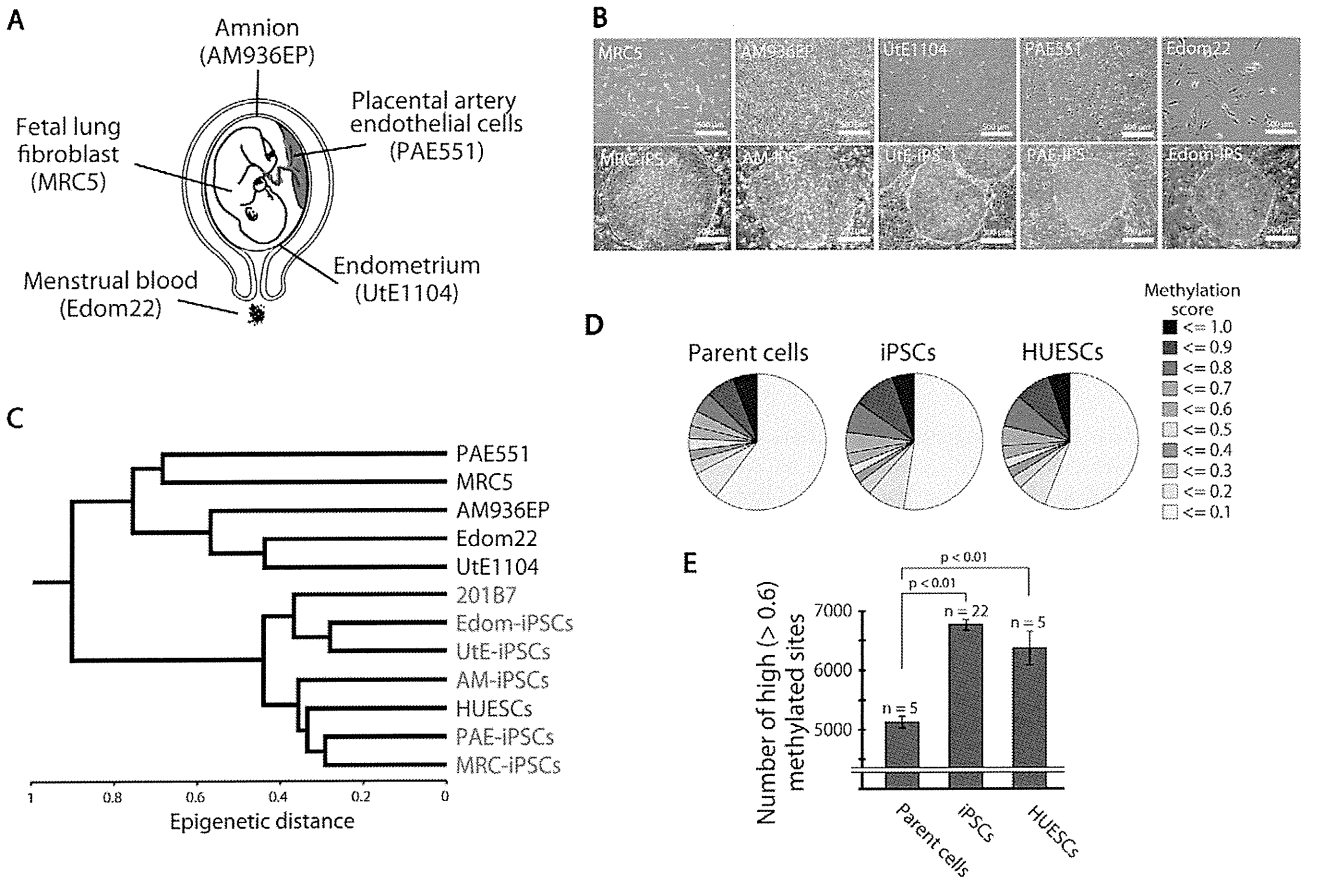

Figure 1. Pluripotent stem cells are significantly more hyper-methylated than their parent cells. (*A*) The human cell origins used for generation of iPSCs. (*B*) Morphology of the parent cells (upper panels) and iPSCs (lower panels). (*C*) Unsupervised hierarchical clustering analysis based on DNA methylation. (*D*) Distribution of 24,273 CpG sites with their methylation scores in the parent cells, iPSCs and ESCs. (*E*) The average number of high (>0.6) methylated CpG sites. The iPSCs have more highly methylated sites than the parent cells.
doi:10.1371/journal.pgen.1002085.g001

S5). The distribution of DNA methylation levels shows that the degree of global methylation in pluripotent stem cells was higher compared to the parent cells (Figure 1D, 1E), suggesting that a global gain of DNA methylation occurs during reprogramming.

Identification of stem cell-specific differentially methylated regions (DMRs)

For further analysis, we defined DMR as representing a CpG site whose score differed 0.3 points or more from the β-value between the two groups. By comparison among ESCs (average from 5 lines), iPSCs (average from 22 lines), and parent cells (average from 5 lines), about 90% of the CpG sites (17,572 sites) examined did not show differential methylation among ESCs, iPSCs and parent cells (Figure 2A), suggesting that only a small number of the CpG sites is affected during reprogramming. The number of the CpG sites has been reported to be larger by genome-wide analysis [21].

We then identified 220 sites that are pluripotent stem cell-specific DMRs (Figure 2A). The 174 sites (79.5%) of the stem cell-specific DMRs had significantly higher methylation levels in iPSCs/ESCs when compared to the parent cells (Figure 2B). Approximately 80% of the DMRs between the iPSCs and their parent cells changed to a "hyper-methylated" state from a "hypo-methylated" state in iPSCs. In contrast, 45 sites of the stem cell-specific DMRs are hypo-methylated in iPSCs/ESCs, compared with the parent cells. Gene ontology analysis indicates that the hypo-methylated stem cell-specific DMRs especially included genes related to mRNA transcription regulation (Figure 2B). Interestingly, the majority of the hypo-methylated stem cell-specific DMRs were located on CpG islands, whereas the majority of the hyper-methylated stem cell-specific DMRs were located on non-CpG islands (Figure 2C). No iPS-specific DMRs were detected. We extracted 3,123 sites that are differentially methylated in one or more parent-specific iPSCs, compared to their parent cells, because DMRs are dependent on parent cell types (Figure S6). These DMRs are here designated as stem cell-required DMRs. Distribution analysis of the stem cell-required DMRs revealed a dispersed pattern rather than specific localization on the genome (Figure S7A).

From the combined gene expression and DNA methylation data, we chose 27 genes in the stem cell-specific DMRs showing more than a 5-fold change in expression of human iPSCs/ESCs, as compared with those in the parent cells (Table S4). Nine genes with hypo-methylated stem cell-specific DMRs were found in the group "genes significantly expressed in iPSCs/ESCs," and 17 genes with hypo-methylated stem cell-specific DMRs belonged to the category "low expression or silenced in iPSCs/ESCs". In addition, the methylation state and gene expression in *EPHA1*, *PTPN6*, *RAB25*, *SALL4*, *GBP3*, *LYST*, *SP100* and *UBE1L* were confirmed by quantitative combined bisulfite restriction analysis (COBRA) [25] (Figure 2D), RT-PCR (Figure 2E) and bisulfite sequencing (Figure 2F).

We also extracted genes with stem cell-required DMRs exhibiting high expression or suppression in human iPSCs/ESCs (Tables S5, S6). Interestingly, gene ontology analysis of the genes with stem cell-required DMRs showed that genes in the transcription factor category were detected only in the hypo-methylated stem cell-required DMRs (Table S7). The top 20 transcription factor genes with hypo-methylated stem cell-required DMRs exhibiting high expression in human iPSCs are summarized in Table 1 and include *OCT-4/3* (also known as *POU5F1*), *SALL4*, *SOX8*, *ZIC5*, and *FOXD1*.

Aberrant and inherited methylation in iPSCs

Few changes in DNA methylation were detected between iPS and ES cells and these were not consistent among the different iPS lines (Figure 2A, Figures S6, S7). In further analyses, we compared the DNA methylation states of each iPSC line or each parent cell line with that of ESCs (averaged value) (Figure 3A). For the whole genome, the number of DMRs between ESCs and iPSCs (ES-iPS-DMRs) varied in the 22 iPSC lines (Figure 3B). A comprehensive analysis of methylation in ESCs and iPSCs identified 1,459 ES-iPS-DMRs covering 1,260 genes that were differentially methylated in one or more iPSC lines. ES-iPS-DMRs are composed of aberrant (iPS-specific) methylation sites, in comparison with ESCs and inherited methylation sites from the parent cells. The number of inherited sites as well as aberrant sites varied among iPSCs. Analysis of the ES-iPS-DMRs on each chromosome showed a characteristic distribution of the ES-iPS-DMRs on the X chromosome in XX-iPSCs (Figure 3B and Figure S8). Female XX-iPSCs demonstrate a tendency to carry a large number of ES-iPS-DMRs on the X chromosome, but male XY-iPSCs had few ES-iPS-DMRs on the X chromosome (Figure 3B, lower panel). While no ES-iPS-DMRs overlapped for all the iPSCs (Figure 2A), 20 ES-iPS-DMRs overlapped in more than 15 out of 22 lines (Figure 3C, inset). These 20 ES-iPS-DMRs include the genes for *MPG* (N-methylpurine-DNA glycosylase isoform b), *FZD10* (frizzled 10), *IREX2* (iroquois homeobox protein 2) and *ZNF248* (zinc finger protein 248), which are highly associated with aberrant methylation during reprogramming. Distribution analysis of the ES-iPS-DMRs across the genome did not show any specific localization (Figure S9). We further compared overlapping ES-iPS-DMRs in reference to a genome-wide methylation analysis [21], and found that 72 gene promoters overlapped between our data and that of Lister et al..

More than 70% of the ES-iPS-DMRs were hyper-methylated in each iPSC (Figure 3D), indicating that the iPSC genome is more methylated than the ESC genome. In addition, the majority of the ES-iPS-DMRs were located on CpG islands (Figure 3E), suggesting that aberrant methylation is biased towards CpG islands.

Effect of long-term culture on DNA methylation status in iPSCs

We investigated the effect of continuous passaging on the DNA methylation profile of human iPSCs. To address the effect, we subjected 7 iPSC lines to additional rounds of passaging under identical culture conditions, and obtained genomic DNA and RNA at passage 4 (P4) to P40 for DNA methylation and gene expression. The number of the ES-iPS-DMRs ranged from 80 in MRC-iPS-25 to 286 in UtE-iPS-11 at early passage (P10 to P20), whereas the number of the ES-iPS-DMRs dramatically decreased in all lines at late passage (P30 to P40) (Figure 4A, upper-left panel). The number of inherited and aberrant sites decreased to 30 and 70, respectively, at P30 to P40 (Figure 4A, upper-center and right panels). These decreases in the numbers of ES-iPS-DMRs indicate that iPSCs have become closer to ESCs in their DNA methylation profiles. In particular, XX-iPSC lines (AM-iPS-8, UtE-iPS-4 and -11, and Edom-iPS-2) showed decreases in the number of ES-iPS-DMRs with passaging. The XY-iPSC lines, such as MRC-iPS-25 and PAE-iPS-1, had only a small number of ES-iPS-DMRs. The number of ES-iPS-DMRs continued to decrease to approximately 100 ES-iPS-DMRs containing 30 inherited sites. Intriguingly, few ES-iPS-DMRs on the X chromosome were detected in XY-iPSCs throughout the passaging. In contrast, the number of ES-iPS-DMRs in XX-iPSCs ranged from 10 to 70 at the early passage (P4 to P20), and decreased to zero after P30 (Figure 4A, lower panels). We also

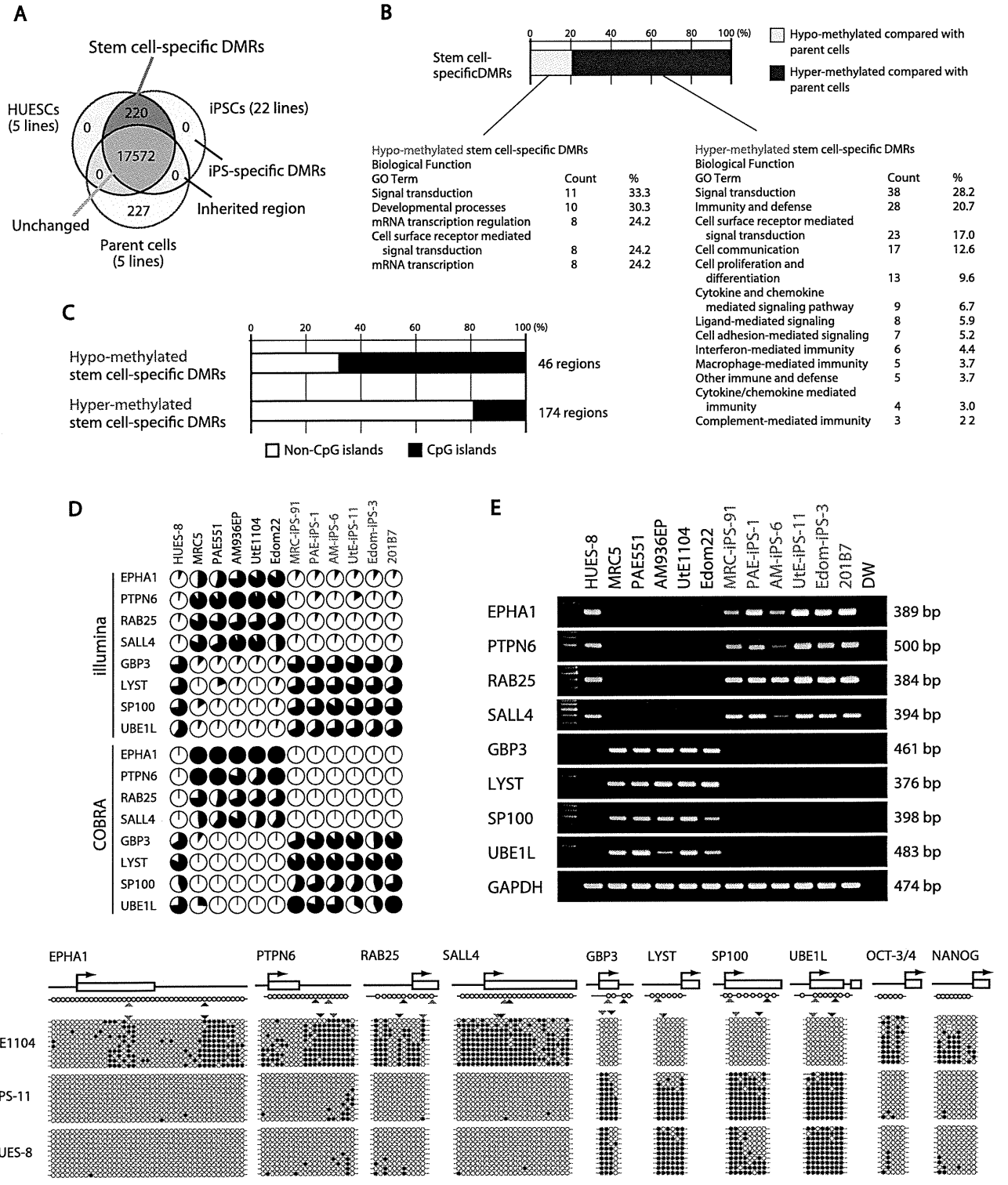

Figure 2. Defining stem cell-specific DMRs as novel epigenetic iPS markers. (*A*) Venn-like diagram showing overlapping CpG sites among ESCs, iPSCs and their parent cells. The 220 overlapping sites are stem cell-specific differentially methylated regions (DMRs). Notably, neither overlapping iPSCs-specific DMRs nor inherited regions in iPSCs from the parent cells were observed. (*B*) Proportion of the hyper- and hypo-methylated stem cell-specific DMRs and GO analysis. Approximately 80% of the regions were hyper-methylated in iPSCs, compared with that of the parent cells. (*C*) Proportion of the regions associated with CpG islands and non-CpG islands in the hypo-methylated stem cell-specific DMRs. The hypo-methylated regions were biased to CpG islands, whereas the hyper-methylated regions were biased to non-CpG islands. (*D*) DNA methylation levels in the 8 representative genes determined by Illumina Infinium HumanMethylation27 assay and Bio-COBRA. These 8 genes were defined as SS-DMRs with significant changes of expression and were described in Table S6. The relative amount of methylated and unmethylated DNA ratio is indicated as the black and white area, respectively, in the pie chart. (*E*) Expression of the 8 genes. Expression of the 8 genes had an inverse correlation with DNA methylation level. (*F*) Bisulfite sequencing analysis of the 8 genes in endometrial cells (UtE1104), UtE-iPS-11 and HUES-8 cells. (Top)

Schematic diagram of the genes. Arrows, open boxes and open circles represent transcription start site, first exon and position of CpG sites, respectively. (Bottom) Open and closed circles indicate unmethylated and methylated sites, respectively. Red and blue arrowheads represent the position of CpG sites in Infinium assay and COBRA assay, respectively.
doi:10.1371/journal.pgen.1002085.g002

investigated the effect of continuous passaging on the DNA methylation profile of the parent cells (UtE1104 and Edom22) (Figure 4B). The number of the DMRs between ESCs and parent cells (ES-parent-DMRs) increased with passaging. In addition, we also confirmed that the transgenes were silenced at each passage (Figure 4C and Figure S4), indicating that the decreasing number of the ES-iPS-DMRs in iPSCs occurred in the transgene-independent phase.

Comparative analysis of ES-iPS-DMRs dynamics

We then compared each ES-iPS-DMRs with passaging. The UtE-iPS-11 had 286 ES-iPS-DMRs at P13, 194 sites at P18, 110 sites at P31, and 55 sites at P39. The ES-iPS-DMRs detected at P13 decreased with passaging (blue bars in upper-left panel in Figure 5A). Interestingly, 66 de novo ES-iPS-DMRs appeared at P18, while at P13 these sites showed no differences between UtE-iPS-11 and ESCs (orange bars in upper-left panel in Figure 5A). These 66 ES-iPS-DMRs also decreased with passaging (P31 and P39). The 29 additional ES-iPS-DMRs at P31 also appeared and decreased with passaging (P39) (green bars in upper-left panel in Figure 5A) and 16 ES-iPS-DMRs at P39 (red bar in upper-left panel in Figure 5A) appeared. Rapid appearance and gradual disappearance of ES-iPS-DMRs was a recurring theme, but the number of newly-appearing ES-iPS-DMRs decreased with passaging (Figure 5A, upper-left panel). The same change in ES-iPS-DMRs occurred on the X chromosome, but the number of the ES-iPS-DMRs approached zero at early passages (Figure 5A, upper-center panel). Intriguingly, this change also occurred at inherited sites, which was contrary to our expectations. The inherited sites also repeatedly appeared and disappeared, and the number of newly-appearing inherited sites decreased with passaging (Figure 5A, upper-right panel). The term "inherited" is here used to mean the same methylation state found in iPSCs and their parent cells, but the "inherited" regions behaved like "aberrant" regions that had multiple appearances and disappearances. These multiple appearances/disappearances of ES-iPS-DMRs were observed in all iPSC lines regardless of parental cell type. The ES-parent-DMRs were also analyzed. The *de novo* ES-parent-DMRs appeared as well as the ES-iPS-DMRs, but did not decrease with passaging (Figure 5B).

Most ES-iPS-DMRs were hyper-methylated in iPSCs

ES-iPS-DMRs can be categorized into two groups: a, hyper-methylated and b, hypo-methylated sites in iPSCs, as compared

Table 1. List of the top 20 out of 82 transcription factor genes with hypo-methylated stem cell-required DMRs exhibiting "high" expression in human iPS cells.

		DNA methylation		
TargetID	**Gene name**	**HUESCs**	**iPSCs**	**Expression level**
cg13083810	POU5F1, POU domain; class 5; transcription factor 1 isoform 1	0.584	0.549	55543.9
cg06303238	SALL4, sal-like 4	0.032	0.026	29766.2
cg16990174	RYBP, RING1 and YY1 binding protein	0.076	0.119	10274.1
cg03589001	MORF4L1, MORF-related gene 15 isoform 2	0.176	0.173	7015.7
cg02204046	MYCN, v-myc myelocytomatosis viral related oncogene; neuroblastoma derived	0.022	0.027	5826.8
cg10705800	CITED4, Cbp/p300-interacting transactivator; with Glu/Asp-rich carboxy-terminal domain; 4	0.438	0.445	5342.2
cg21696393	SOX8, SRY (sex determining region Y)-box 8	0.074	0.061	1976.7
cg23131007	TCF12, transcription factor 12 isoform b	0.138	0.155	1930.7
cg18808261	SATB1, special AT-rich sequence binding protein 1	0.194	0.242	1634.4
cg15607672	OTX2, orthodenticle 2 isoform a	0.046	0.054	1227.5
cg05345286	MDFI, MyoD family inhibitor	0.023	0.040	1035.9
cg20909686	OVOL1, OVO-like 1 binding protein	0.215	0.204	991.0
cg26209676	ZNF581, zinc finger protein 581	0.113	0.196	916.1
cg05522383	PITX2, paired-like homeodomain transcription factor 2 isoform b	0.024	0.030	544.8
cg17675150	ZNF532, zinc finger protein 532	0.069	0.107	525.3
cg01510051	ZNF542, zinc finger protein 542	0.585	0.555	443.9
cg06154570	HEYL, hairy/enhancer-of-split related with YRPW motif-like	0.134	0.152	440.3
cg12556134	TGIF2, TGFB-induced factor 2	0.075	0.072	405.4
cg03663715	FOXD1, forkhead box D1	0.030	0.042	349.1
cg09721427	HHEX, hematopoietically expressed homeobox	0.077	0.101	206.9

"Expression level" is an average of raw data values in iPSCs from Gene Chip data.
doi:10.1371/journal.pgen.1002085.t001

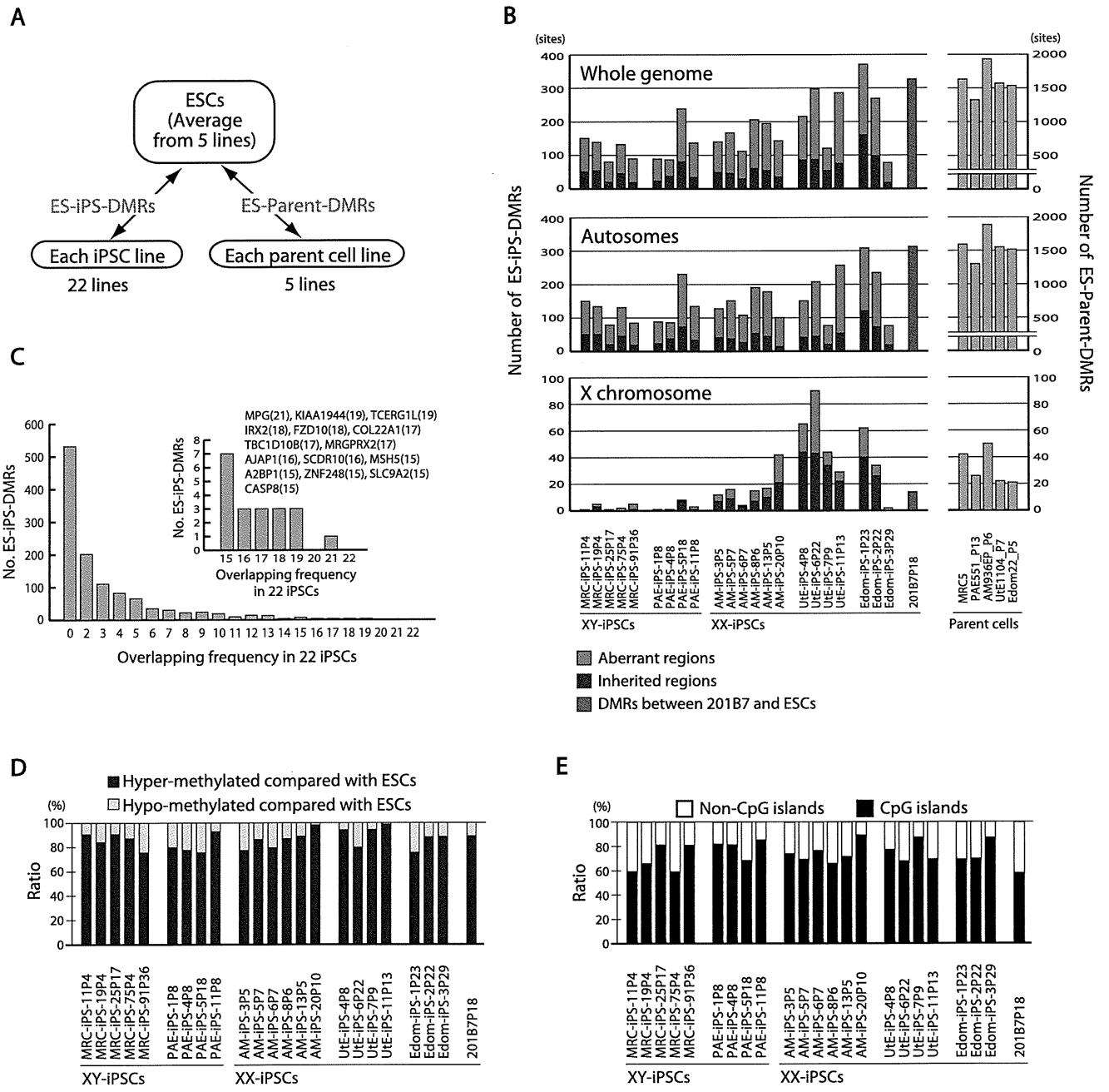

Figure 3. Aberrant methylation in human iPSCs. (*A*) Comparison of DNA methylation states of each iPSC line or each parent cell line with that of ESCs. The DMRs between ESCs and iPSCs are designated as ES-iPS-DMRs, and the DMRs between ESCs and parent cells are designated as ES-parent-DMRs. (*B*) The number of ES-iPS-DMRs and ES-parent-DMRs on whole genome (top), autosomes (middle) and X chromosome (bottom). Ratios of number of inherited regions in iPSCs from parent cells (blue) and aberrant regions in iPSCs that differ from ESCs and parent cells (red) in the ES-iPS-DMRs are shown in bars. Female iPSCs were demonstrated to carry high number of EiP-DMRs on X chromosome. (*C*) Number of overlapped ES-iPS-DMRs frequency in iPSCs. No overlapping ES-iPS-DMRs in all 22 iPSC lines. (Inlet) A small number of overlapping ES-iPS-DMRs of the frequency from 15 to 22. Overlapping frequency of each gene is indicated in parentheses. (*D*) Proportion of the hyper- and hypo-methylated ES-iPS-DMRs. More than 75% of the ES-iPS-DMRs were hyper-methylated in iPSCs. (*E*) Proportion of the ES-iPS-DMRs associated with CpG islands and non-CpG islands in ach iPSC line. ES-iPS-DMRs were biased to CpG islands.
doi:10.1371/journal.pgen.1002085.g003

with ESCs. ES-iPS-DMRs that disappeared at the last passage (P39) (blue bars in Figure 5) in both UtE-iPS-11 and Edom-iPS-2 were extracted, and each methylation score of the extracted ES-iPS-DMRs is shown (Figure 6, upper and middle panels). To compare methylation scores, a "difference value" was estimated by subtracting the scores of ESCs from those of each cell (Figure 6, lower panels). Positive and negative difference values indicate that these sites are hyper- and hypo-methylated, respectively, when compared with ESCs. Difference values of the ES-iPS-DMRs showing aberrant methylation states in iPSCs at the early passage approached zero with passaging. It should be noted that the almost all difference values became largely positive in iPSCs at

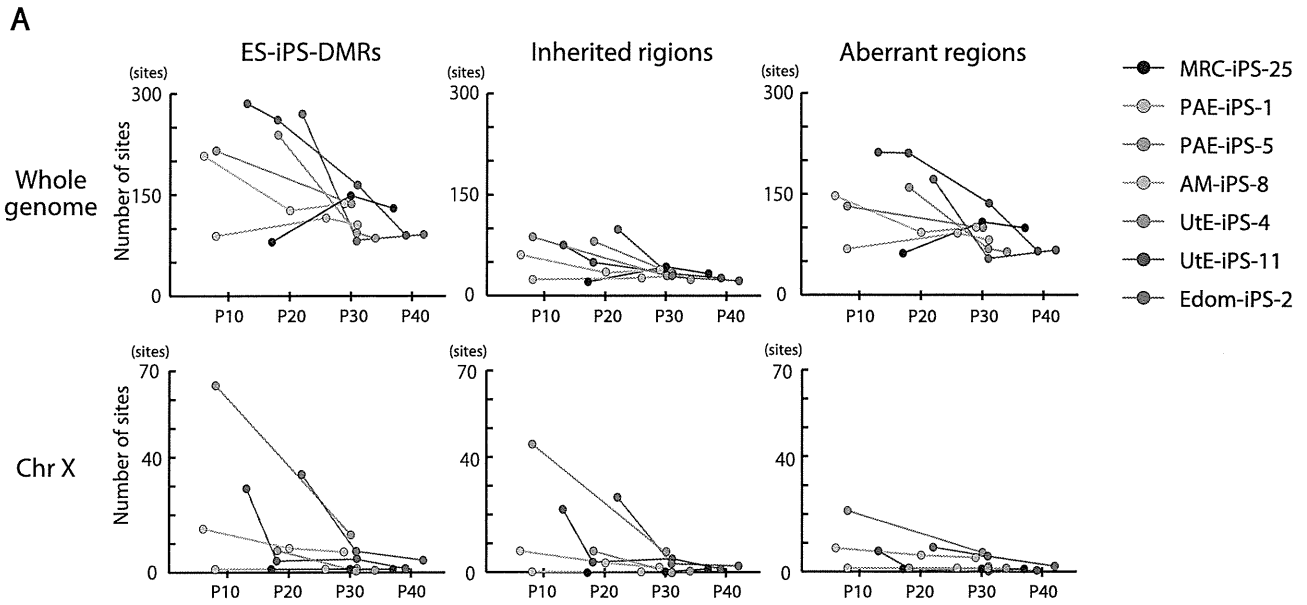
A
ES-iPS-DMRs
Inherited rigions
Aberrant regions
Whole genome
Chr X
(sites)
Number of sites
300
150
0
70
40
P10
P20
P30
P40
MRC-iPS-25
PAE-iPS-1
PAE-iPS-5
AM-iPS-8
UtE-iPS-4
UtE-iPS-11
Edom-iPS-2

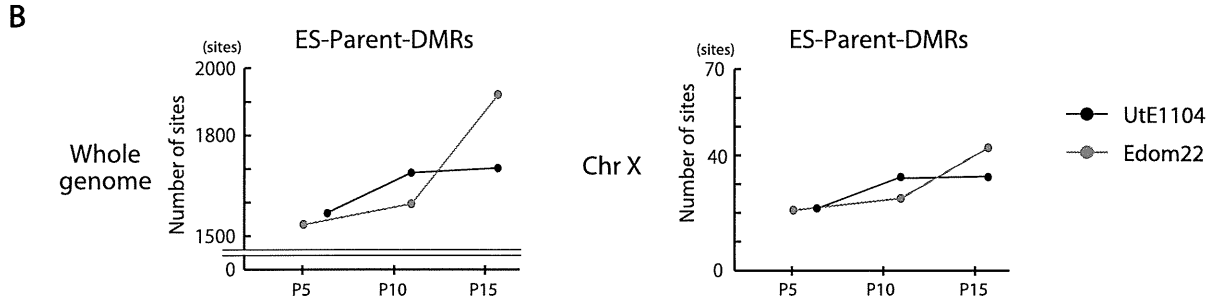
B
ES-Parent-DMRs
ES-Parent-DMRs
Whole genome
Chr X
(sites)
Number of sites
2000
1800
1500
0
70
40
P5
P10
P15
UtE1104
Edom22

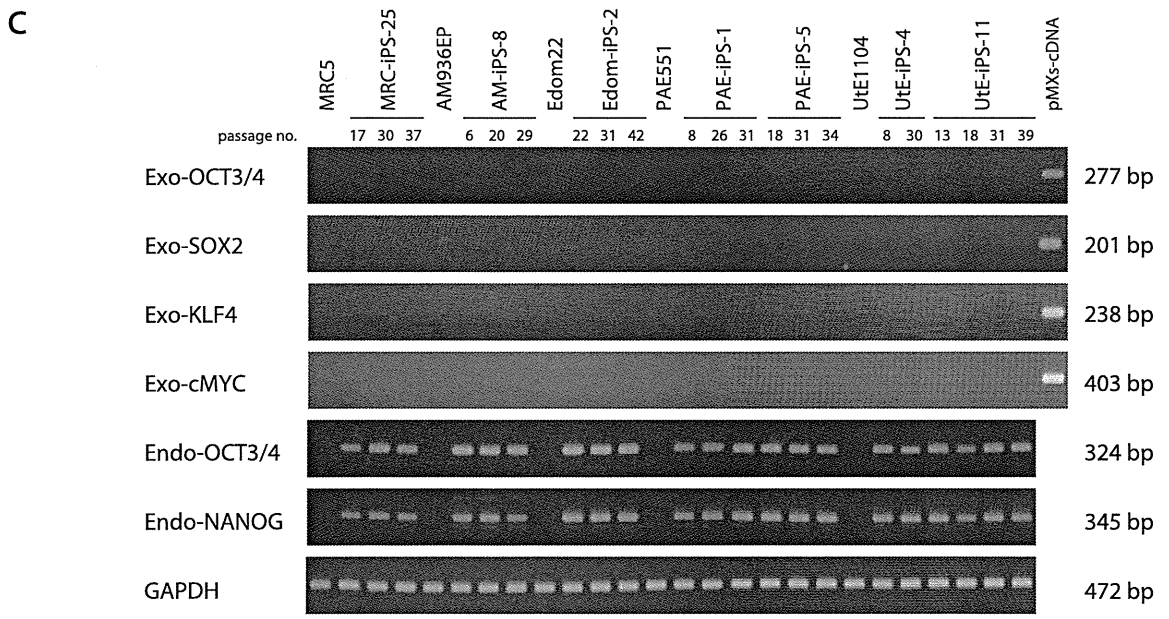
C
MRC5
MRC-iPS-25
AM936EP
AM-iPS-8
Edom22
Edom-iPS-2
PAE551
PAE-iPS-1
PAE-iPS-5
UtE1104
UtE-iPS-4
UtE-iPS-11
pMXs-cDNA
passage no.
17 30 37
6 20 29
22 31 42
8 26 31
18 31 34
8 30
13 18 31 39
Exo-OCT3/4
Exo-SOX2
Exo-KLF4
Exo-cMYC
Endo-OCT3/4
Endo-NANOG
GAPDH
277 bp
201 bp
238 bp
403 bp
324 bp
345 bp
472 bp

Figure 4. Effect of long-term cultivation on ES-iPS-DMRs. (*A*) Decrease in the number of the ES-iPS-DMRs with continuous passaging. Upper panels show change of the number of the ES-iPS-DMRs (left), the inherited regions (middle) and aberrant regions (right) on whole genome. Lower panels show change in the number of the ES-iPS-DMRs (left), inherited regions (middle) and aberrant regions (right) on X chromosome. The number of the ES-iPS-DMRs in XX-iPSCs approached zero with continuous passaging on X chromosome. In contrast, XY-iPSCs had few ES-iPS-DMRs on X chromosome throughout the passages. (*B*) The number of the ES-parent-DMRs with continuous passaging. (*C*) No expression of the transgenes in iPSCs at each passage was detected by RT-PCR.
doi:10.1371/journal.pgen.1002085.g004

early passage (P13 or P22), even though they were negative in the parent cells, and then approached zero upon further passaging. This transiently-induced hyper-methylation was observed at each passage in all iPSC lines examined. The observed transient hypermethylation patterns during iPS reprogramming did not correspond to methyflated CpGs in the parental cells. However, this observation does not rule out that transient aberrant methylation could also be observed in some cases on sites that were methylated in the parental cells.

Discussion

Identification of novel epigenetic iPS markers

OCT-4/3 and *NANOG* have been used as epigenetic markers for iPSCs [8–10,26,27]. We previously showed candidate epigenetic markers by analyzing 6 iPS lines [17]. Here we identified 8 novel epigenetic markers more closely by defining 9 genes with the hypo-methylated stem cell-specific DMRs and significantly higher expression, and 17 genes with the hyper-methylated stem cell-specific DMRs and significantly lower expression in iPSCs/ESCs from 22 iPS lines. DNA methylation and expression of these genes, especially the 8 genes, *SALL4*, *EPHA1*, *PTPN6*, *RAB25*, *GBP4*, *LYST*, *SP100* and *UBE1L*, can now be used as epigenetic markers for pluripotent stem cells. Among these 8 genes, *SALL4* has been used as an expression marker, and is revealed for the first time as an epigenetic marker. These epigenetic changes during reprogramming can be detected by 3 different methods (Illumina assay, COBRA and bisulfite sequencing), and is evident, i.e. CpG sites are methylated or unmethylated in an all-or-none fashion. The identification of these novel epigenetic markers can be another tool for the validation of pluripotent stem cells that are iPSCs and ESCs.

The hypo-methylated stem cell-required DMRs may have an important role for reprogramming as do the stem cell-specific DMRs, because reprogramming is dependent on the type of parent cells. In fact, genes associated with the hypo-methylated stem cell-required DMRs include a large number of transcription factors that are involved in pluripotency. Establishment of the stem cell-required DMRs database in iPSCs derived from different types of parent cells can help to generate human iPSCs in a fast and easy manner. Hypo-methylated stem cell-specific regions have been reported to be abundant in CpG islands [28–30]. In this study, the hypo-methylated stem cell-specific DMRs were significantly biased towards CpG islands, whereas the hyper-methylated stem cell-specific DMRs were biased to non-CpG islands, suggesting that genes with CpG islands have a propensity to be demethylated during reprogramming towards pluripotent stem cells. The higher number of the hyper-methylated stem cell-specific DMRs in iPSCs indicates that the Yamanaka factors activate only limited numbers of stem cell-specific/associated genes through demethylation of the specific DMRs shown in this study on the genome in parallel with methylating most genes associated with tissue-specific function during reprogramming.

Multiple appearances/disappearances of aberrant hyper-methylation

Continuous passaging of iPSCs reduces differences among clones in gene expression profiles in mouse [15] and in human [31] cells. Here we detected multiple appearances and disappearances of aberrant hyper-methylation throughout iPSC reprogramming. Furthermore, human iPSCs were gradually reprogrammed through the "convergence" of periodic aberrant hyper-methylation upon continuous passaging (Figure 7). The term "convergence" is used here to mean that amplitude of aberrant hyper-methylation (or number of ES-iPS-DMRs) decreases. The decrease of aberrant methylation suggests that iPSCs lose the characteristics inherited from the parent cells and adapt to ESCs. This aberrant and stochastic hyper-methylation and their convergence may be a direct cause of the transgene-independent phases of iPS reprogramming [15]. Aberrant hyper-methylation, for which the mechanism remains unclear, can possibly be attributed, at least in part, to up-regulation of DNMT3B, a de novo methyltransferase, at the early stages of reprogramming.

Maintenance of an epigenetic memory of their parent cells at early passage of human iPSCs (Figure 4A) is consistent with recent reports involving mouse iPSCs [15–17]. However, most inherited sites from the parent cells in iPSCs were inconsistent among iPSC clones from the same parent cells on the genome, and these sites showed periodic aberrant hyper-methylation during passaging, as well as aberrant sites. Inherited methylation is non-synchronous and stochastic, much like aberrant methylation, rather than deterministic. The inherited sites thus comprise a portion of all aberrant methylation observed in the clones.

Mouse female iPSCs as well as mouse female ESCs carry two active X chromosomes [32], but inactivation of the X chromosome in human female ESCs is variable [22,33–35]. It has been reported recently that human female iPSCs show a variable state of X-inactivation as is seen in human female ESCs [22,36]. In this study, human iPSCs exhibited a dynamic epigenetic state on the X chromosome. The ES-iPS-DMRs on the X chromosome in XY-iPSCs were rare and the average number of ES-iPS-DMRs in XY-iPSCs was significantly lower than in XX-iPSCs, suggesting that iPSCs are prone to aberrant hyper-methylation on the inactive X chromosome. A recent report showed that X inactivation in human ESCs is sensitive to the level of oxygen through culture in vitro [35]. Therefore, analysis of aberrant methylation in iPSCs that are established and cultured in low oxygen condition would be help to understand physiological relevance of X inactivation and reprogramming.

Incomplete adaptation of iPSCs to ESCs

The number of passages for "convergence" of the aberrant hyper-methylation seems be dependent on parental cell types and their sex. Disappearance of iPSCs in culture within 10 passages is occasionally observed, regardless of the cell of origin. This instability may be due to an excess of aberrant hyper-methylation at early passages in addition to the "partial reprogramming" theory [15]. The late-passage iPSCs, like the early-passage iPSCs, retained the ability to differentiate into cell types found in all three germ layers. iPSCs showed reduced aberrant methylation during adaptation to ESCs; however, iPSCs retained approximately 100 aberrant sites on autosomes, implying that iPSCs do not become identical to ESCs, although they become very close. The remaining aberrant sites were inconsistent among iPSC clones

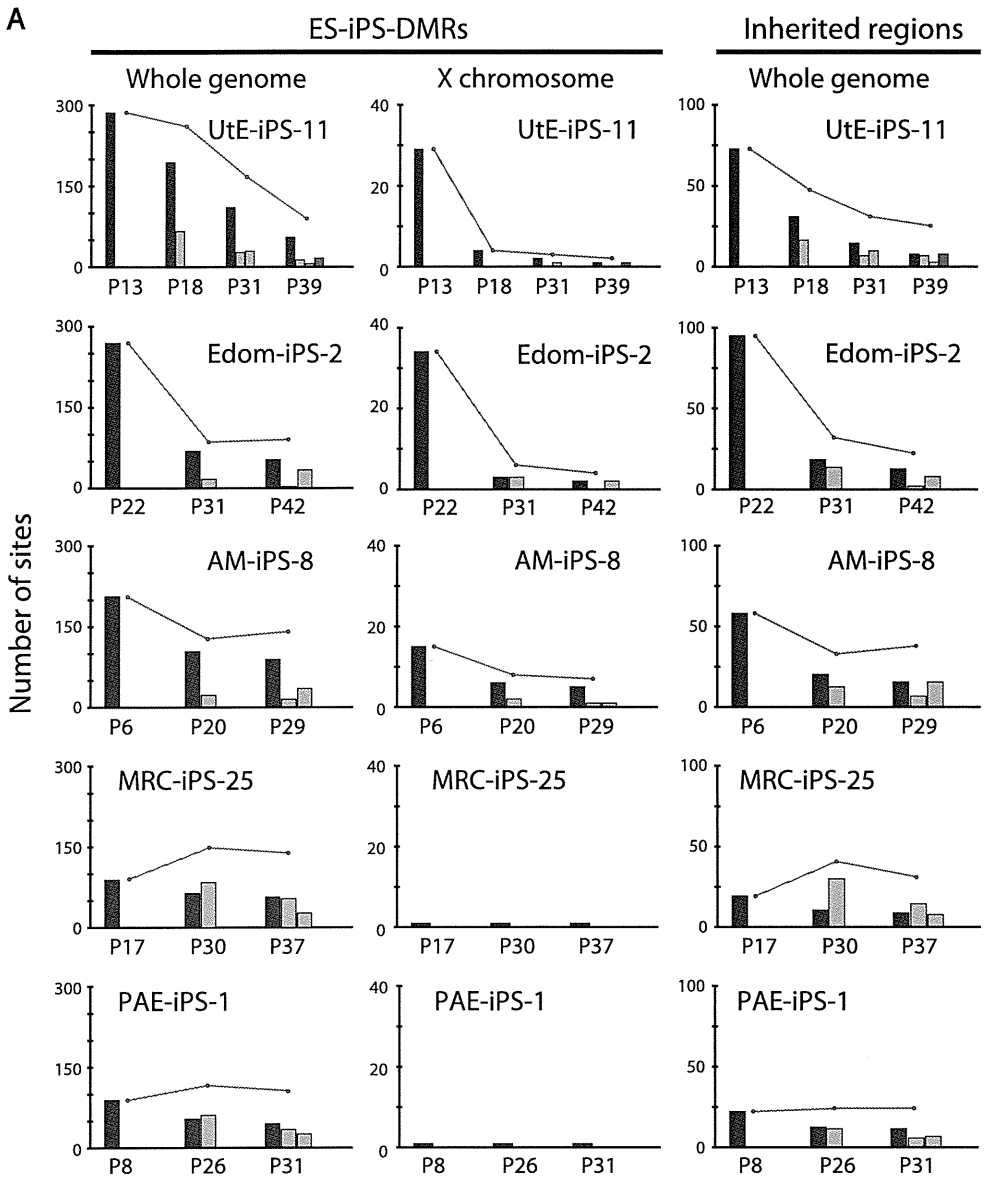
A
ES-iPS-DMRs
Inherited regions
Whole genome
X chromosome
Whole genome
Number of sites
UtE-iPS-11
Edom-iPS-2
AM-iPS-8
MRC-iPS-25
PAE-iPS-1
P13 P18 P31 P39
P22 P31 P42
P6 P20 P29
P17 P30 P37
P8 P26 P31

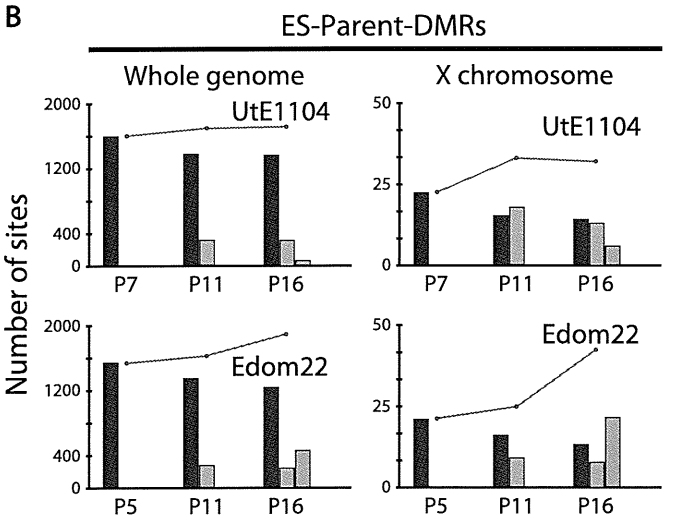
B
ES-Parent-DMRs
Whole genome
X chromosome
Number of sites
UtE1104
Edom22
P7 P11 P16
P5 P11 P16

Figure 5. Number of the ES-iPS-DMRs and ES-parent-DMRs with passaging. (*A*) Number of the ES-iPS-DMRs with passaging. Red line plots indicate total number of the ES-iPS-DMRs. Blue bars indicate the number of the ES-iPS-DMRs that appeared at the earliest passage. Orange, green and red bars indicate the number of the ES-iPS-DMRs that appeared secondarily at later passages. Appearance/disappearance of the ES-iPS-DMRs and inherited regions were repeated, but the number of newly-appeared ES-iPS-DMRs was decreased with passaging. (*B*) Number of the ES-parent-DMRs with passaging. Blue bars indicate the number of the ES-parent-DMRs at P5 (or P7). Orange and green bars indicate de novo ES-parent-DMRs at P11 and P16, respectively.
doi:10.1371/journal.pgen.1002085.g005

with different parent cell types, but the numbers were consistent among iPSC clones after a 42-week cultivation. The quantity (or number) of ES-iPS-DMRs would be another validation index for iPSC identity as well as quality analysis (or methylation ratio) of pluripotent stem cell-specific methylation.

Abnormalities of imprint genes, *MEG3* genes, and *H19* genes in human iPSCs

Genomic imprinting of *H19*, *IGF2* and *MEG3* has been reported to be unstable in human ESCs [37,38]. The *Dlk1-Dio3* genes were aberrantly silenced in most of the mouse iPSC lines. But mouse iPSCs without *MEG3* expression still have the ability to differentiate into cell type of three germ layers *in vitro* [39]. In humans, IG-DMR and MEG3-DMR are relevant to upd(14)pat-like and upd(14)mat-like phenotypes [40]. In this study, only *MEG3* and *H19*, out of 87 imprinted genes examined showed aberrant methylation in human iPSCs (Figure S10). Six out of 15 human iPSC lines were aberrantly methylated at MEG3-DMR. *MEG3* expression was silenced in those six lines regardless of their parent cell type, although all parent cells showed about 50% methylation at MEG3-DMR and expression of *MEG3* (Figure S10A, S10B). However, MEG3-negative iPS lines are almost indistinguishable from MEG3-positive iPS lines in DNA methylation and gene expression in human. Continuous passaging

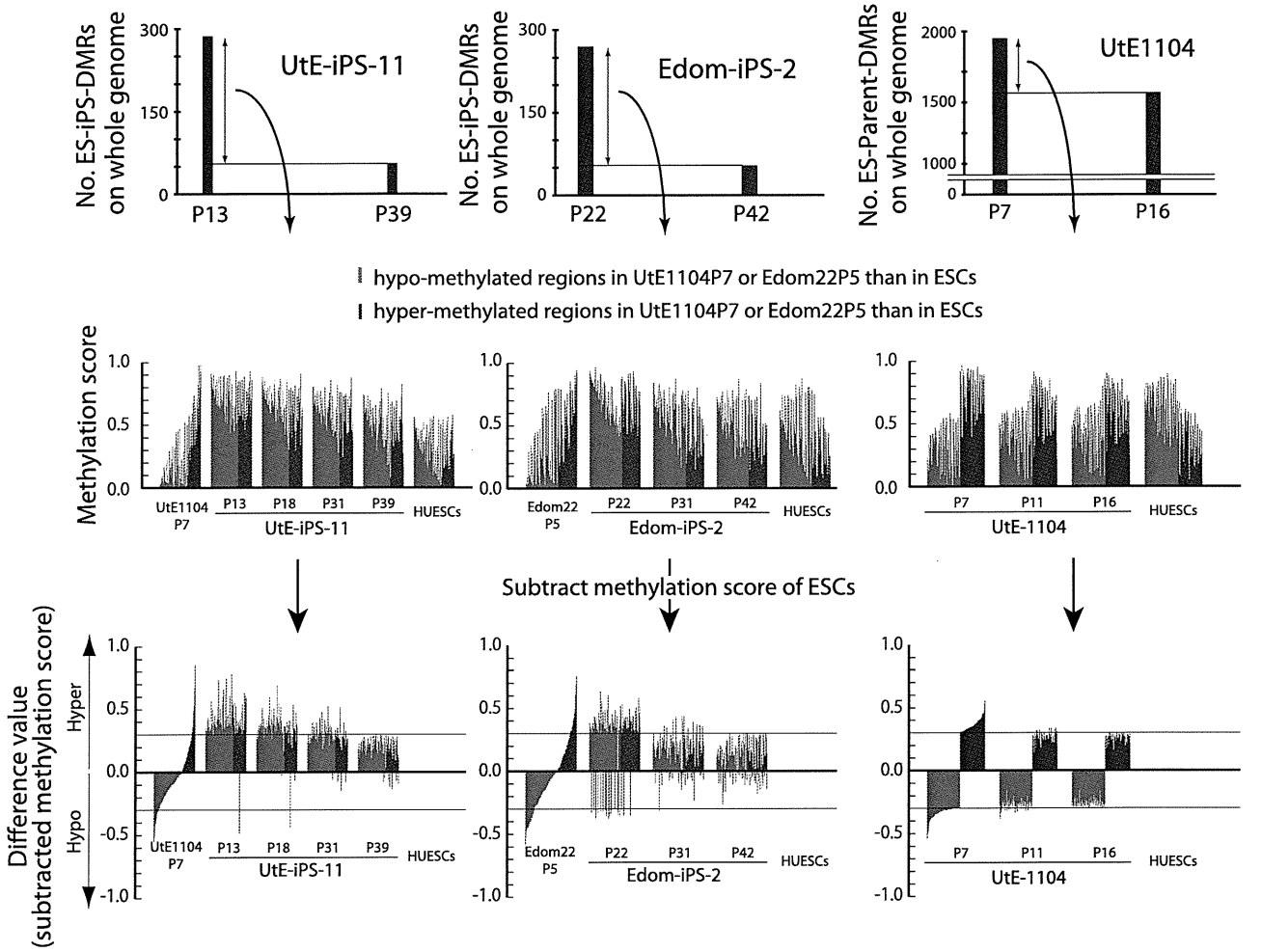

Figure 6. Hyper-methylation in the ES-iPS-DMRs and ES-parent-DMRs. ES-iPS-DMRs that disappeared in UtE-iPS-11 and Edom-iPS-2 at the latest passage (upper) were analyzed and the methylation score of each ES-iPS-DMR was plotted on bar graph (middle). To clearly compare methylation scores, difference value were estimated by subtracting the scores of ESCs from that of each sample (lower). Red and blue bars represent hypo- and hyper-methylated regions, respectively, in the parent cells, compared with ESCs. Notably, almost all the regions, even though their difference values were hypo-methylated in the parent cells, became hyper-methylated in iPSCs at the early passage, and then their methylation levels were adjusted to the level of ESCs with passaging, i.e. subtracted methylation score became close to zero. This transiently-induced hyper-methylation was not detected in parent cells.
doi:10.1371/journal.pgen.1002085.g006

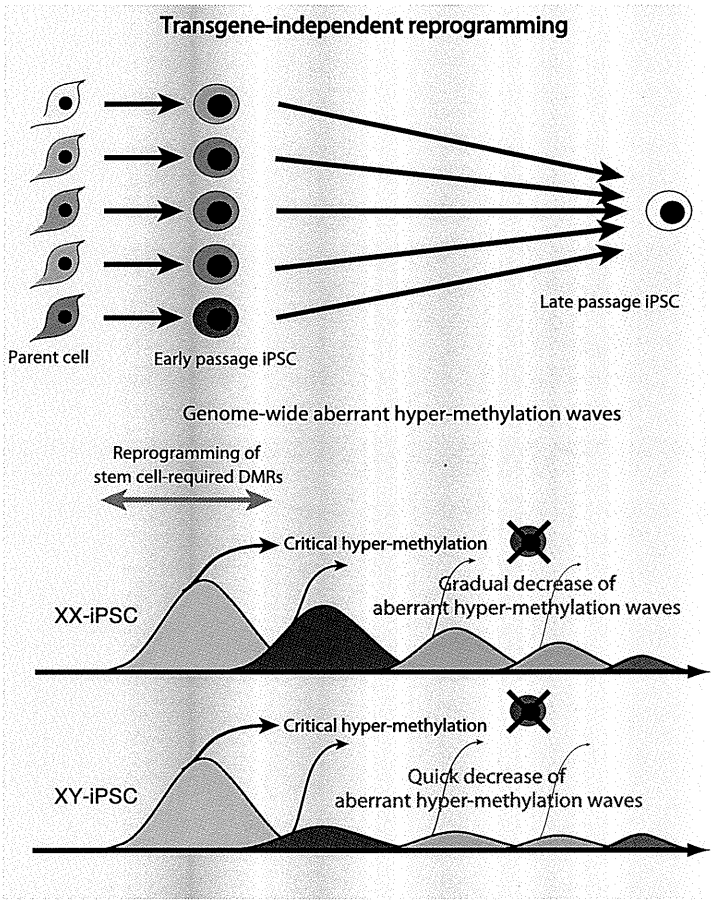

Figure 7. Model of mechanism for transgene-independent reprogramming. During reprogramming from somatic cells to iPSCs, the cells undergo dynamic change of methylation of SS-DMRs and genome. The cells with incomplete reprogramming or excessive hyper-methylation of the genome fail to maintain pluripotency at early passages. Human iPSCs are transgene-independently reprogrammed gradually through "convergence" of periodic aberrant hyper-methylation and become closer to ESCs upon continuous passaging. Due to the sensitivity to aberrant methylation on X chromosome, XY-iPSCs become close to ESCs faster than XX-iPSCs do.
doi:10.1371/journal.pgen.1002085.g007

did not resolve the aberrant hyper-methylation at MEG3-DMR, suggesting that these abnormalities occur at early passage and are fixed at later stages. In addition, aberrant hyper-methylation at *H19* in all iPSCs and ESCs was observed (Figure S10C), and *H19* was not expressed in all iPSCs and their parent cells.

We revealed that transgene-independent reprogramming is a convergence of periodic hyper-methylation. The aberrant hyper-methylation in iPSCs occurs stochastically throughout the genome. Early-stage iPSC clones with different propensities due to stochastic hyper-methylation may be used after selection of desirable phenotypes to treat a wide range of target diseases using cell-based therapy, and would thus have advantages for clinical use. In this sense, the number of ES-iPS-DMRs and methylation states of the stem cell-specific DMRs are useful epigenetic indices for evaluating human iPSCs in therapeutic applications.

Materials and Methods

Ethics statement

Human endometrium, amnion, placental artery endothelium and menstrual blood cells were collected by scraping tissues from surgical specimens, under signed informed consent, with ethical approval of the Institutional Review Board of the National Institute for Child Health and Development, Japan. Signed informed consent was obtained from donors, and the surgical specimens were irreversibly de-identified. All experiments handling human cells and tissues were performed in line with Tenets of the Declaration of Helsinki.

Human cell culture

Endometrium (UtE1104), amnion (AM936EP), placental artery endothelium (PAE551) and menstrual blood cell (Edom22) cell lines were independently established in our laboratory [41,42]. UtE1104, AM936EP, Edom22, and MRC-5 [43] cells were maintained in the POWEREDBY10 medium (MED SHIROTORI CO., Ltd, Tokyo, Japan). PAE551 cells were cultured in EGM-2MV BulletKit (Lonza, Walkersville, MD, USA) containing 5% FBS. Human iPSCs were generated in our laboratory, via procedures described by Yamanaka and colleagues [8] with slight modification [17,41,44–46]. The human cells were infected with retroviruses produced from the retroviral vector pMXs, which encodes the cDNA for human *OCT3/4*, *SOX2*, *c-MYC*, and *KLF4*. Human iPSCs were established from MRC-5, AM936EP, UtE1104, and PAE551, which were designated as MRC-iPSCs, AM-iPSCs, UtE-iPSCs and PAE-iPSCs [17,41,44–46]. Edom-iPSCs were established from Edom22 in this study. Human iPSCs were maintained on irradiated MEFs in 0222 medium (MED SHIROTORI CO., Ltd, Tokyo, Japan) supplemented with

10 ng/ml recombinant human basic fibroblast growth factor (bFGF, Wako Pure Chemical Industries, Ltd., Osaka, Japan). The 201B7 human iPSC line [8] that was generated from human skin fibroblasts by retroviral transfection with 4 transcription factors was also used. Frozen pellets of human ESCs (HUESCs) [23,24] were kindly gifted from Drs. C. Cowan and T. Tenzan (Harvard Stem Cell Institute, Harvard University, Cambridge, MA).

DNA methylation analysis

DNA methylation analysis was performed using the Illumina infinium assay with the HumanMethylation27 BeadChip (Illumina) and the BeadChip was scanned on a BeadArray Reader (Illumina), according to the manufacturer's instructions. Methylated and unmethylated signals were used to compute a β-value, which was a quantitative score of DNA methylation levels, ranging from "0", for completely unmethylated, to "1", for completely methylated. On the HumanMethylation27 BeadChip, oligonucleotides for 27,578 CpG sites covering more than 14,000 genes are mounted, mostly selected from promoter regions. CpG sites with ≥0.05 "Detection p value" (computed from the background based on negative controls) were eliminated from the data for further analysis, leaving 24,273 CpGs (13,728 genes) valid for use with the 51 samples tested. Average of methylation was calculated from HUESCs, MRC-iPSCs, AM-iPSCs, UtE-iPSCs, PAE-iPSCs and Edom-iPSCs, in which DMRs among each line in the each set were removed. Analyzed data sets (list of stem cell-specific DMRs and stem cell-required DMRs) can be obtained from http://www.nch.go.jp/reproduction/e/thdmds.html.

Gene expression analysis

Gene expression analysis was performed using the Agilent Whole Human Genome Microarray chips G4112F (Agilent, Santa Clara, CA), which contains over 41,000 probes. Raw data were normalized and analyzed by GeneSpringGX11 software (Silicon Genetics, Redwood City, CA). For RT-PCR, an aliquot of total RNA was reverse-transcribed using Random Hexamer primers. The cDNA template was amplified using specific primers for *EPHA1*, *PTPN6*, *RAB25*, *SALL4*, *GBP3*, *LYST*, *SP100*, *UBE1L*, OCT3/4 and NANOG. For detecting RNA derived from transgenes, specific primer sets, FY-11 and OCT3/4-SR, FY-11 and SOX2-SR, KLF4-SF and FY-12, cMYC-SF and FY-12, were used. Expression of glyceraldehyde-3-phosphate dehydrogenase (GAPDH) was used as a control. Primers used in this study are summarized in Table S8.

Quantitative combined bisulfite restriction analysis (COBRA) and bisulfite sequencing

To confirm the DNA methylation state, bisulfite PCR-mediated restriction mapping (known as the COBRA method) was performed. Sodium bisulfite treatment of genomic DNA was carried out using EZ DNA Methylation-Gold kit (Zymo Research). PCR amplification was performed using BIOTAQ HS DNA polymerase (Bioline Ltd; London, UK) with specific primers for *EPHA1*, *PTPN6*, *RAB25*, *SALL4*, *GBP3*, *LYST*, *SP100*, and *UBE1L*. Primers used in this study are summarized in Table S8. After digestion with restriction enzymes, HpyCH4IV or Taq I, quantitative-COBRA coupled with the Shimadzu MCE-202 MultiNA Microchip Electrophoresis System (Shimadzu, Japan) was carried out for quantitative DNA methylation level. To determine the methylation state of individual CpG sites, the PCR product was gel extracted and subcloned into pGEM T Easy vector (Promega, Madison, WI), and then sequenced. The promoter regions of the *OCT3/4* and *NANOG* [41,44] were also amplified and sequenced. Methylation sites were visualized and quality control was carried out by the web-based tool, "QUMA" (http://quma.cdb.riken.jp/) [47].

Web tools

The following web tools were used in this study: NIA Array [48] (http://lgsun.grc.nia.nih.gov/ANOVA/) for hierarchical clustering, DAVID Bioinformatics Resources [49] (http://david.abcc.ncifcrf.gov/home.jsp), PANTHER Classification System [50] (http://www.pantherdb.org/).

Accession numbers

NCBI GEO: HumanMethylation27 BeadChip data and gene expression microarray data have been submitted under accession number GSE 20750, GSE24676 and GSE24677.

Supporting Information

Figure S1 Immunohistochemistry of stem cell-specific surface antigens, NANOG, OCT3/4, SOX2, SSEA-4 and TRA-1-60 in AM-iPSCs, MRC-iPSCs and Edom-iPSCs, and teratoma formation of those iPSCs by subcutaneous implantation into NOD/Scid mice. The iPSCs differentiated to various tissues including ectoderm (neural tissues and retinal pigment epithelium), mesoderm (cartilage) and endoderm (gut). Immunostaining and teratoma formation were carried out as previously described [41,44].
(PDF)

Figure S2 Immunohistochemistry of stem cell-specific surface antigens, NANOG, OCT3/4, SOX2, SSEA-4 and TRA-1-60 in PAE-iPSCs and UtE-iPSCs, and teratoma formation of those iPSCs by subcutaneous implantation into NOD/Scid mice. The iPSCs differentiated to various tissues including ectoderm (neural tissues and retinal pigment epithelium), mesoderm (cartilage) and endoderm (gut). Immunostaining and teratoma formation were carried out as previously described [41,44].
(PDF)

Figure S3 Bisulfite sequencing at the OCT3/4 and NANOG promoter regions in ESCs, iPSCs and their parent cells.
(PDF)

Figure S4 Expression of the transgenes in iPSCs. (A) RT-PCR for transgenes in 22 iPSC lines. No expression of the transgenes in each iPSC lines was detected. (B) Quantitative RT-PCR for the transgenes at each passage. Relative expression of each transgene normalized to GAPDH was calculated. P0(D2), RNA from UtE1104 cells that were infected with the retroviruses and were cultured for 2 days. No expression of the transgenes at each passage was detected.
(PDF)

Figure S5 (A) Unsupervised hierarchical clustering analysis based on DNA methylation (left) and gene expression (right) in each ESC line, iPSC line and their parent cell line. (B) Unsupervised hierarchical clustering analysis based on DNA methylation (left) and gene expression (right) of average of ESCs, iPSCs and parent cells. (C) Scatter plot of DNA methylation (left) and gene expression data (right) in ESCs, iPSCs and their parent cells.
(PDF)

Figure S6 (A) Venn-like diagram showing seven categories (aa-gg) overlapped CpG sites among ESCs, iPSCs and their parent cells. (B) Number of CpG sites involved in each seven category from the five ESCs-iPSCs-the parent cell sets. "Overlapped"

indicates a number of sites that overlap in all iPSCs examined. The 220 overlapping sites in "ee" are designated as stem cell-specific differentially methylated regions (DMRs) and 3,123 total sites in "ee" are designated as stem cell-required DMRs. Notably, no overlapping sites were observed in "bb" that is a category involved in iPSCs-specific DMRs and in "ff" that is a category involved in inherited regions in iPSCs from the parent cells.
(PDF)

Figure S7 (A) Distribution of stem cell-required DMRs on each chromosome (upper) and frequency on each chromosome (bottom). (B) The number of parent cell specific DMRs (left) and the number of iPSC derived from different parent cells specific DMRs (left).
(PDF)

Figure S8 The number of DMRs between ESCs and each iPSC line (ES-iPS-DMRs) on each chromosome. ES-iPS-DMRs between 201B7 (iPSCs from Yamanaka) and ESCs are shown for comparison.
(PDF)

Figure S9 Distribution of the ES-iPS-DMRs on each chromosome. Distribution of the EiP-DMRs overlapped in less than 9 lines (light blue bars), in more than 10 and less than 14 lines (blue bars), and in more than 15 lines (red bars) among 22 lines.
(PDF)

Figure S10 DNA methylation at human *MEG3* and *H19*. (A) DNA methylation at MEG3-DMR (CG7) and expression of MEG3. (Top) Schematic diagram of the MEG3 gene. The arrow, open boxes and open circles represent transcription start site, first exon and position of CpG sites, respectively. Red and blue arrowheads represent the position of CpG sites in Infinium assay and COBRA assay, respectively. DNA methylation scores of MEG3 were determined by Illumina Infinium HumanMethylation27 assay (upper bar graph) and Bio-COBRA (lower bar graph). (Bottom) Expression of MEG3 and GAPDH was determined by RT-PCR. Information of MEG3 primers for COBRA and RT-PCR is described by Kagami et al. [40]. (B) Bisulfite sequencing analysis of MEG3-DMRs (CG7). (C) Methylation scores of H19 were determined by Illumina Infinium HumanMethylation27 assay.
(PDF)

Table S1 List of human cells analyzed for a methylation state in this study.
(PDF)

Table S2 STR analysis of iPSCs.
(PDF)

Table S3 Karyotypic analysis of iPSCs.
(PDF)

Table S4 List of genes with stem cell-specific DMRs exhibiting significant changes in expression in human iPS cells.
(PDF)

Table S5 List of the top 100 genes with hypo-methylated stem cell-required DMRs exhibiting 'high' expression in human iPS cells.
(PDF)

Table S6 List of top 100 genes with hyper-methylated stem cell-required DMRs exhibiting suppression in human iPS cells.
(PDF)

Table S7 List of top 5 categories of GO Term in "Stem cell-required DMRs".
(PDF)

Table S8 Primer list.
(PDF)

Acknowledgments

We would like to express our sincere thanks to Drs. C. Cowan and T. Tenzan for HUESC lines; to Drs. K. Hata and K. Nakabayashi for COBRA; to Dr. H. Makino for establishing the AM936EP, UtE1104, PAE551, and Edom22 cells; to Mr. M. Machida for immunohistochemical analysis; to Ms. Y. Takahashi for bioinformatics analyses; and Dr C. Ketcham for critical proofreading.

Author Contributions

Conceived and designed the experiments: KN AU. Performed the experiments: KN MT MY-I. Analyzed the data: KN. Contributed reagents/materials/analysis tools: KN MT MY-I YF EC HS HA. Wrote the paper: KN AU.

References

1. Li E (2002) Chromatin modification and epigenetic reprogramming in mammalian development. Nat Rev Genet 3: 662–673.
2. Reik W (2007) Stability and flexibility of epigenetic gene regulation in mammalian development. Nature 447: 425–432.
3. Feng S, Jacobsen SE, Reik W (2010) Epigenetic reprogramming in plant and animal development. Science 330: 622–627.
4. Hattori N, Nishino K, Ko YG, Ohgane J, Tanaka S, et al. (2004) Epigenetic control of mouse Oct-4 gene expression in embryonic stem cells and trophoblast stem cells. J Biol Chem 279: 17063–17069.
5. Hattori N, Imao Y, Nishino K, Ohgane J, Yagi S, et al. (2007) Epigenetic regulation of Nanog gene in embryonic stem and trophoblast stem cells. Genes Cells 12: 387–396.
6. Nishino K, Hattori N, Tanaka S, Shiota K (2004) DNA methylation-mediated control of Sry gene expression in mouse gonadal development. J Biol Chem 279: 22306–22313.
7. Zingg JM, Pedraza-Alva G, Jost JP (1994) MyoD1 promoter autoregulation is mediated by two proximal E-boxes. Nucleic Acids Res 22: 2234–2241.
8. Takahashi K, Tanabe K, Ohnuki M, Narita M, Ichisaka T, et al. (2007) Induction of pluripotent stem cells from adult human fibroblasts by defined factors. Cell 131: 861–872.
9. Yu J, Vodyanik MA, Smuga-Otto K, Antosiewicz-Bourget J, Frane JL, et al. (2007) Induced pluripotent stem cell lines derived from human somatic cells. Science 318: 1917–1920.
10. Park IH, Zhao R, West JA, Yabuuchi A, Huo H, et al. (2008) Reprogramming of human somatic cells to pluripotency with defined factors. Nature 451: 141–146.
11. Woltjen K, Michael IP, Mohseni P, Desai R, Mileikovsky M, et al. (2009) piggyBac transposition reprograms fibroblasts to induced pluripotent stem cells. Nature 458: 766–770.
12. Park IH, Arora N, Huo H, Maherali N, Ahfeldt T, et al. (2008) Disease-specific induced pluripotent stem cells. Cell 134: 877–886.
13. Miura K, Okada Y, Aoi T, Okada A, Takahashi K, et al. (2009) Variation in the safety of induced pluripotent stem cell lines. Nat Biotechnol 27: 743–745.
14. Ghosh Z, Wilson KD, Wu Y, Hu S, Quertermous T, et al. (2010) Persistent donor cell gene expression among human induced pluripotent stem cells contributes to differences with human embryonic stem cells. PLoS ONE 5: e8975. doi:10.1371/journal.pone.0008975.
15. Polo JM, Liu S, Figueroa ME, Kulalert W, Eminli S, et al. (2010) Cell type of origin influences the molecular and functional properties of mouse induced pluripotent stem cells. Nat Biotechnol 28: 848–855.
16. Kim K, Doi A, Wen B, Ng K, Zhao R, et al. (2010) Epigenetic memory in induced pluripotent stem cells. Nature.
17. Nishino K, Toyoda M, Yamazaki-Inoue M, Makino H, Fukawatase Y, et al. (2010) Defining Hypo-Methylated Regions of Stem Cell-Specific Promoters in Human iPS Cells Derived from Extra-Embryonic Amnions and Lung Fibroblasts. PLoS ONE 5: e13017. doi:10.1371/journal.pone.0013017.
18. Fazzari MJ, Greally JM (2004) Epigenomics: beyond CpG islands. Nat Rev Genet 5: 446–455.
19. Fazzari MJ, Greally JM (2010) Introduction to epigenomics and epigenome-wide analysis. Methods Mol Biol 620: 243–265.

20. Doi A, Park IH, Wen B, Murakami P, Aryee MJ, et al. (2009) Differential methylation of tissue- and cancer-specific CpG island shores distinguishes human induced pluripotent stem cells, embryonic stem cells and fibroblasts. Nat Genet 41: 1350–1353.
21. Lister R, Pelizzola M, Kida YS, Hawkins RD, Nery JR, et al. (2011) Hotspots of aberrant epigenomic reprogramming in human induced pluripotent stem cells. Nature 471: 68–73.
22. Bock C, Kiskinis E, Verstappen G, Gu H, Boulting G, et al. (2011) Reference Maps of Human ES and iPS Cell Variation Enable High-Throughput Characterization of Pluripotent Cell Lines. Cell 144: 439–452.
23. Cowan CA, Klimanskaya I, McMahon J, Atienza J, Witmyer J, et al. (2004) Derivation of embryonic stem-cell lines from human blastocysts. N Engl J Med 350: 1353–1356.
24. Osafune K, Caron L, Borowiak M, Martinez RJ, Fitz-Gerald CS, et al. (2008) Marked differences in differentiation propensity among human embryonic stem cell lines. Nat Biotechnol 26: 313–315.
25. Brena RM, Auer H, Kornacker K, Plass C (2006) Quantification of DNA methylation in electrofluidics chips (Bio-COBRA). Nat Protoc 1: 52–58.
26. Takahashi K, Yamanaka S (2006) Induction of pluripotent stem cells from mouse embryonic and adult fibroblast cultures by defined factors. Cell 126: 663–676.
27. Huangfu D, Osafune K, Maehr R, Guo W, Eijkelenboom A, et al. (2008) Induction of pluripotent stem cells from primary human fibroblasts with only Oct4 and Sox2. Nat Biotechnol 26: 1269–1275.
28. Fouse SD, Shen Y, Pellegrini M, Cole S, Meissner A, et al. (2008) Promoter CpG methylation contributes to ES cell gene regulation in parallel with Oct4/Nanog, PcG complex, and histone H3 K4/K27 trimethylation. Cell Stem Cell 2: 160–169.
29. Meissner A, Mikkelsen TS, Gu H, Wernig M, Hanna J, et al. (2008) Genome-scale DNA methylation maps of pluripotent and differentiated cells. Nature 454: 766–770.
30. Sato S, Yagi S, Arai Y, Hirabayashi K, Hattori N, et al. (2010) Genome-wide DNA methylation profile of tissue-dependent and differentially methylated regions (T-DMRs) residing in mouse pluripotent stem cells. Genes Cells 15: 607–618.
31. Chin MH, Pellegrini M, Plath K, Lowry WE (2010) Molecular analyses of human induced pluripotent stem cells and embryonic stem cells. Cell Stem Cell 7: 263–269.
32. Maherali N, Sridharan R, Xie W, Utikal J, Eminli S, et al. (2007) Directly reprogrammed fibroblasts show global epigenetic remodeling and widespread tissue contribution. Cell Stem Cell 1: 55–70.
33. Hall LL, Byron M, Butler J, Becker KA, Nelson A, et al. (2008) X-inactivation reveals epigenetic anomalies in most hESC but identifies sublines that initiate as expected. J Cell Physiol 216: 445–452.
34. Shen Y, Matsuno Y, Fouse SD, Rao N, Root S, et al. (2008) X-inactivation in female human embryonic stem cells is in a nonrandom pattern and prone to epigenetic alterations. Proc Natl Acad Sci U S A 105: 4709–4714.
35. Lengner CJ, Gimelbrant AA, Erwin JA, Cheng AW, Guenther MG, et al. (2010) Derivation of pre-X inactivation human embryonic stem cells under physiological oxygen concentrations. Cell 141: 872–883.
36. Tchieu J, Kuoy E, Chin MH, Trinh H, Patterson M, et al. (2010) Female human iPSCs retain an inactive X chromosome. Cell Stem Cell 7: 329–342.
37. Rugg-Gunn PJ, Ferguson-Smith AC, Pedersen RA (2005) Epigenetic status of human embryonic stem cells. Nat Genet 37: 585–587.
38. Rugg-Gunn PJ, Ferguson-Smith AC, Pedersen RA (2007) Status of genomic imprinting in human embryonic stem cells as revealed by a large cohort of independently derived and maintained lines. Hum Mol Genet 16 Spec No. 2: R243–251.
39. Stadtfeld M, Apostolou E, Akutsu H, Fukuda A, Follett P, et al. (2010) Aberrant silencing of imprinted genes on chromosome 12qF1 in mouse induced pluripotent stem cells. Nature 465: 175–181.
40. Kagami M, Sekita Y, Nishimura G, Irie M, Kato F, et al. (2008) Deletions and epimutations affecting the human 14q32.2 imprinted region in individuals with paternal and maternal upd(14)-like phenotypes. Nat Genet 40: 237–242.
41. Nagata S, Toyoda M, Yamaguchi S, Hirano K, Makino H, et al. (2009) Efficient reprogramming of human and mouse primary extra-embryonic cells to pluripotent stem cells. Genes Cells 14: 1395–1404.
42. Cui CH, Uyama T, Miyado K, Terai M, Kyo S, et al. (2007) Menstrual blood-derived cells confer human dystrophin expression in the murine model of Duchenne muscular dystrophy via cell fusion and myogenic transdifferentiation. Mol Biol Cell 18: 1586–1594.
43. Jacobs JP, Jones CM, Baille JP (1970) Characteristics of a human diploid cell designated MRC-5. Nature 227: 168–170.
44. Makino H, Toyoda M, Matsumoto K, Saito H, Nishino K, et al. (2009) Mesenchymal to embryonic incomplete transition of human cells by chimeric OCT4/3 (POU5F1) with physiological co-activator EWS. Exp Cell Res 315: 2727–2740.
45. Saito S, Onuma Y, Ito Y, Tateno H, Toyoda M, et al. (2010) Potential linkages between the inner and outer cellular states of human induced pluripotent stem cells. BMC Bioinformatics, in press.
46. Toyoda M, Yamazaki-Inoue M, Itakura Y, Kuno A, Ogawa T, et al. (2010) Lectin microarray analysis of pluripotent and multipotent stem cells. Genes Cells, in press.
47. Kumaki Y, Oda M, Okano M (2008) QUMA: quantification tool for methylation analysis. Nucleic Acids Res 36: W170–175.
48. Sharov AA, Dudekula DB, Ko MS (2005) A web-based tool for principal component and significance analysis of microarray data. Bioinformatics 21: 2548–2549.
49. Huang da W, Sherman BT, Lempicki RA (2009) Systematic and integrative analysis of large gene lists using DAVID bioinformatics resources. Nat Protoc 4: 44–57.
50. Mi H, Lazareva-Ulitsky B, Loo R, Kejariwal A, Vandergriff J, et al. (2005) The PANTHER database of protein families, subfamilies, functions and pathways. Nucleic Acids Res 33: D284–288.

Sato et al. BMC Developmental Biology 2011, 11:22
http://www.biomedcentral.com/1471-213X/11/22

BMC
Developmental Biology

RESEARCH ARTICLE Open Access

Lipid rafts enriched in monosialylGb5Cer carrying the stage-specific embryonic antigen-4 epitope are involved in development of mouse preimplantation embryos at cleavage stage

Ban Sato[1,4], Yohko U Katagiri[1*], Kenji Miyado[2], Nozomu Okino[3], Makoto Ito[3], Hidenori Akutsu[2], Hajime Okita[1], Akihiro Umezawa[2], Junichiro Fujimoto[1], Kiyotaka Toshimori[4] and Nobutaka Kiyokawa[1]

Abstract

Background: Lipid rafts enriched in glycosphingolipids (GSLs), cholesterol and signaling molecules play an essential role not only for signal transduction started by ligand binding, but for intracellular events such as organization of actin, intracellular traffic and cell polarity, but their functions in cleavage division of preimplantation embryos are not well known.

Results: Here we show that monosialylGb5Cer (MSGb5Cer)-enriched raft domains are involved in development during the cleavage stage of mouse preimplantation embryos. MSGb5Cer preferentially localizes at the interfaces between blastomeres in mouse preimplantation embryos. Live-imaging analysis revealed that MSGb5Cer localizes in cleavage furrows during cytokinesis, and that by accumulating at the interfaces, it thickens them. Depletion of cholesterol from the cell membrane with methyl-beta-cyclodextrin (MbCD) reduced the expression of MSGb5Cer and stopped cleavage. Extensive accumulation of MSGb5Cer at the interfaces by cross-linking with anti-MSGb5Cer Mab (6E2) caused F-actin to aggregate at the interfaces and suppressed the localization of E-cadherin at the interfaces, which resulted in the cessation of cleavage. In addition, suppression of actin polymerization with cytochalasin D (CCD) decreased the accumulation of MSGb5Cer at the interfaces. In E-cadherin-targeted embryos, the MSGb5Cer-enriched raft membrane domains accumulated heterotopically.

Conclusions: These results indicate that MSGb5Cer-enriched raft membrane domains participate in cytokinesis in a close cooperation with the cortical actin network and the distribution of E-cadherin.

Background

The molecular dynamics involved in embryogenesis is now being elucidated. In the early cleavage stage of embryogenesis, the localization of cell surface molecules periodically changes and is spatio-temporally controlled. Cytokinesis is a fundamental process of cell cleavage in which the daughter cells split after nuclear division, and it is driven by actin-dependent narrowing of a contractile ring as well as furrow-specific addition of membrane [1,2]. The latter contributes to dynamic rearrangement of cell surface proteins and provides molecules required to construct the complex machinery of cytokinesis. For example, the cell surface adhesion molecule E-cadherin is drastically rearranged in a close correlation with the dynamics of cortical actin [3]. It is well documented that E-cadherin is located predominantly in membrane domains involved in cell-cell contacts of adjacent blastomeres and mediates adhesion between blastomeres of preimplantation mouse embryos from 8-cell stage onwards [4-6].

A new aspect of the cell membrane structures called "lipid rafts" has been postulated [7]. Lipid rafts have been described by Lingwood and Simons as "fluctuating nanoscale assemblies of sphingolipid, cholesterol, and proteins that can be stabilized to coalesce into platforms

* Correspondence: kata@nch.go.jp
[1]Department of Pediatric Hematology and Oncology Research, National Research Institute for Child Health and Development, 2-10-1 Okura, Setagaya-ku, Tokyo 157-8535, Japan
Full list of author information is available at the end of the article

that function in membrane signaling and trafficking" [8]. During cell cleavage in embryogenesis, lipid rafts were shown to play an essential role in central spindle assembly and cleavage furrow ingression [1]. For example, GM1 is a monosialylated ganglio-series glycosphingolipid (GSL), which is most commonly used as a raft marker. The lipid rafts enriched in GM1 at the cleavage furrow were shown to possess signaling machinery that contributes to cytokinesis during the cleavage of sea urchin eggs and mouse preimplantation embryos [9,10].

We recently reported finding that monoclonal antibody (Mab) 6E2 raised against human embryonal carcinoma cell line recognizes the globo-series GSL MSGb5Cer is present at the interfaces between blastomeres of living mouse embryos [11]. MSGb5Cer carries an epitope of stage-specific embryonic antigen-4 (SSEA-4), which expressed only in the early cleavage stage of mouse embryos. Lipid rafts enriched with MSGb5Cer was also reported to interact with E-cadherin in breast cancer cell lines [12]. Therefore, MSGb5Cer is expected to form lipid rafts on mouse preimplantation embryos and play an important role in the process of cleavage division. To elucidate the functional role of MSGb5Cer enriched-lipid rafts in embryogenesis, in this study we investigated the dynamics of MSGb5Cer in preimplantation embryos during the course of early embryonic cleavage.

Results

MSGb5Cer and E-cadherin localize at the interfaces between the blastomeres in mouse preimplantation embryos

MSGb5Cer, E-cadherin, and GM1 were visualized in living mouse preimplantation embryos, and their localizations are shown in the optical slice images in Figure 1A. MSGb5Cer and E-cadherin were stained with Mabs 6E2 and ECCD-2, respectively, and they were localized on the cell surface in dotted form in unfertilized eggs but excluded from the area over the meiotic spindle. GM1, on the other hand, was stained with the cholera toxin B subunit (CTX-B) and had accumulated in a perivitelline space in unfertilized eggs, and its accumulation accelerated after fertilization. Preferential localization of MSGb5Cer and E-cadherin at interfaces between blastomeres was also observed in compacted 8-cell stage embryos, whereas GM1 mainly localized at the outer surface area and only a small amount of GM1 was detected at the interfaces. A part of MSGb5Cer was localized similar to GM1 at the outer surface area of blastomeres. These results indicate that MSGb5Cer and E-cadherin, but not GM1, are similarly distributed in preimplantation embryos.

Next, we enzymatically prepared fluorescence-labeled MSGb5Cer or GM1 and introduced into embryos instead of staining with GSL-specific Mab 6E2 or ligand CTX-B to visualize GSLs on embryos. As shown in the optical slice images in Figure 1B, BODIPY®FL-MSGb5Cer was distributed mainly at the interfaces between blastomeres, whereas BODIPY®FL-GM1 was evenly distributed over the surface and in the perivitelline space. In contrast, BODIPY®FL-C12 fatty acids, as a negative control, were not detected at all. The results coincided with that shown by immunostaining. The prolonged culture of BODIPY®FL-MSGb5Cer-introduced embryo in the presence of 6E2 at the same concentration used for immunostaining in Figure 1A did not affect preferential localization of MSGb5Cer, or did not induce the aggregation of MSGb5Cer (Figure 1C). Therefore, it is indicated that the preferential localization of MSGb5Cer at interfaces is due to spontaneous accumulation of MSGb5Cer at interfaces and is not due to the artifactual aggregation of MSGb5Cer induced by cross-linking with antibody.

MSGb5Cer accumulates in the cleavage furrow of preimplantation embryos during cytokinesis, and then at the interfaces after cytokinesis

Time-lapse images of MSGb5Cer visualized with MSGb5Cer-specific Mab (6E2) are shown in Figure 2A. MSGb5Cer began to accumulate at the site of the future furrow (indicated by the arrow) of the spherical zygote at 150 minutes, and accumulation later accelerated and peaked at 180 minutes. Accumulation at the interface also accelerated, and after peaking at 240 minutes, gradually decreased to the initial level at 360 minutes (Figure 2A, B; see the Movie in additional file 1). The means ± s. d. of the fluorescence intensities in the furrow and at the interface of 6 embryos in the round stage, during cytokinesis, after cytokinesis, and in the late 2-cell stage are shown in Figure 2C. MSGb5Cer accumulated in the furrow at the start of cytokinesis and moved to the interface as cytokinesis proceeded. After cytokinesis, the accumulation was gradually broken, and MSGb5Cer eventually became evenly distributed over the entire cell surface, including the interface.

Overlapping distribution of MSGb5Cer with cholesterol

Cholesterol is known to be an important constituent of lipid rafts. Since MSGb5Cer is thought to be also involved in the formation of raft membrane domains in preimplantation embryos, we examined the distribution of cholesterol with Filipin III in the 6E2-stained and fixed embryos. The merged images of MSGb5Cer and cholesterol showed overlapping localization at the interfaces between blastomeres (Figure 3).

MbCD causes de-compaction and subsequent suppression of cell division

Since cholesterol has been postulated to be an absolute requirement for raft integrity, MbCD, which depletes

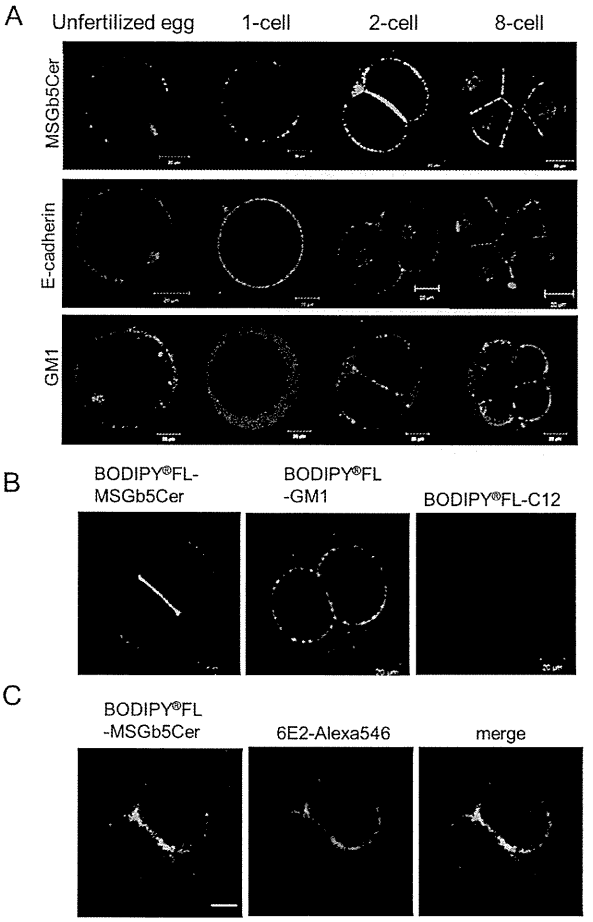

Figure 1 MSGb5Cer localize at the interfaces between blastomeres in mouse preimplantation embryos. (A) Localization of MSGb5Cer, E-cadherin and GM1 in an unfertilized egg and an embryo at the zygote, 2-cell stage and 8-cell stage. MSGb5Cer (top row), E-cadherin (middle row), and GM1 (bottom row) in a living mouse egg or embryos were stained with Alexa Fluor® 488-conjugated 6E2, ECCD-2/Alexa Fluor® 546 Rabbit Anti-rat IgG, and biotinylated-CTX B/Alexa Fluor® 546 streptavidin, respectively, and examined. Thirty sample unfertilized egg and 45 sample embryos of other stages were used for this experiment represented in image. (B) Distribution of BODIPY®FL-MSGb5Cer and BODIPY®FL-GM1 in a 2-cell stage embryo. The distribution of MSGb5Cer and GM1 is shown in the form of optical slice images. BODIPY®FL-C12 fatty acid was used as a negative control. All scale bars represent 20 μm. Ten sample 2-cell stage embryos were used for this experiment represented in each image. (C) Distribution of BODIPY®FL-MSGb5Cer in a 2-cell stage embryo cultured in the presence of 6E2. The BODIPY®FL-MSGb5Cer introduced 2-cell embryo was cultured for 1 hour in M16 medium containing 15 μg/ml of 6E2, and then stained with Alexa Fluor® 546-conjugated 6E2. Scale bar represent 20 μm. Ten sample 2-cell stage embryos were used for this experiment represented in image.

cholesterol from the cell surface, has been used as a tool in lipid raft research [13-15]. To investigate the correlation between raft integrity and the distribution of MSGb5Cer, GM1, and E-cadherin in the embryos, compacted 8-cell embryos were pretreated with various concentrations of MbCD for 15 minutes and then examined. As shown in Figure 4A, pretreatment of the embryos with 0.5 mM MbCD induced decompaction and decreased expression of MSGb5Cer at the interface between blastomeres. The expression on the outer membrane of blastomeres was not decreased and rather seemed to be increased. At a higher concentration (5 mM), expression of MSGb5Cer on the cell surface was further reduced, whereas expression of GM1 and E-cadherin was unaffected. The green fluorescence signals detected in the zona pellucida of 5 mM MbCD-treated embryos are thought to be derived from MSGb5Cer released from the embryo. Treatment with 10 mM MbCD caused complete loss of MSGb5Cer, and decreased expression of GM1, but there were no change in E-cadherin expression.

Next, we investigated the importance of raft integrity in viability of embryos. Pretreatment of 8-cell embryos with MbCD suppressed normal development in a time- and concentration-dependent manner (Figure 4B, C). All embryos in the control culture survived and developed normally into blastocysts by 48 hours of culture, whereas none of embryos pretreated with 0.5 mM MbCD had survived

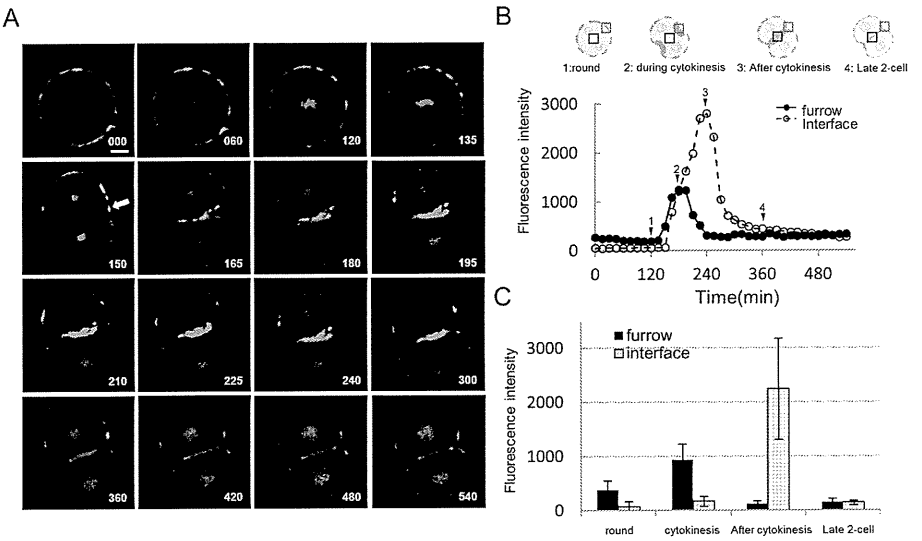

Figure 2 MSGb5Cer accumulates at the interface during cytokinesis in preimplantation embryos. (A) Frames from a series of confocal time-lapse movies of live cytokinesis-stage cells stained with 6E2 for MSGb5cer (green) and with DAPI for nuclei (red). Frames are shown at 60-minute intervals from 0 to 120 minutes, 15-minute intervals from 120 minutes to 240 minutes, and 60-minute intervals from 240 minutes to 540 minutes. Time is expressed in minutes after the start of culture. The arrow at 150 minutes points to the site of a future furrow in the spherical zygote. Scale bar represents 20 μm. The images shown are representative of nine sample zygotes. (B) Temporal changes in fluorescence intensity at the furrow and the interface region during cytokinesis. The fluorescence intensity in pixel values was measured in boxes of equal size located at the furrow (red square) and the interface (black square) of the frames taken every 15 minutes from a confocal time-lapse movie of the zygote of Figure 2A. The fluorescence intensity values at the furrows (closed circles) and interface (open circles) were plotted against time in minutes. Schematic embryos at the round stage (1), during cytokinesis (2), after cytokinesis (3), and the late 2-cell stage (4) were cultured for 105 minutes, 165 minutes, 240 minutes, and 405 minutes, respectively. This data shown is representative of nine sample zygotes. (C) The fluorescence intensity of MSGb5Cer at the furrow (closed column) and interface (dotted column) in round, cytokinesis, post-cytokinesis and late 2-cell stage embryos. Mean values and s.d. were calculated from the results obtained from the time-lapse movies of 6 embryos shown in Figure 2B.

by 48 hours of culture. These results suggest that MSGb5Cer is more sensitive than GM1 to raft integrity, and that lipid raft is prerequisite to cell adhesion and normal development of preimplantation embryos.

Extensive accumulation of MSGb5Cer to interfaces is related to delay and suppression of normal development

As shown in Figure 5A, incubation for 1 hour in the presence of 100 μg/ml of anti- MSGb5Cer Mab 6E2, but not of the isotype-matched control Mab 15B2, led to extensive accumulation of MSGb5Cer at the interfaces in the embryos, and a large aggregate of BODIPY®FL-MSGb5Cer was found.

Prolonged culture of 2-cell embryos in the presence of 6E2 caused a decrease in survival rate, and more than 90% of the embryos died before developing into blastocysts (Figure 5B). 80% of embryos were died after 12 hour culture in 6E2, whereas all of embryos cultured in control Mabs were alive. After 24 hour-culture, embryos cultured in 6E2 cleaved abnormally, and their cleavage rate was delayed as compared with those cultured in control Mabs. The morula embryo, which was able to avoid being injured, seemed to be compacted (arrow in 48 hour culture in 6E2). The anti-MSGb5Cer Mab 6E2 we used in this study is not toxic and do not have non-specific effects on preimplantation embryos, because 100 μg/ml of 6E2 antibody does not affect viability of blastocyst stage embryos that no longer express MSGb5Cer (see Figure S1 in additional file 2). In addition, when either the isotype-matched control Mab 15B2 or anti-E-cadherin Mab ECCD-2 was similarly tested, they did not affect viability of embryos (Figure 5).

Figure 3 MSGb5Cer is overlapped by cholesterol at the interface in a 2-cell embryo. A two-cell stage embryo was stained with 6E2 for MSGb5cer (green) and then filipin III for cholesterol (blue) as described in Materials and Methods. Scale bar: 20 μm. Ten sample 2-cell stage embryos were used for this experiment represented in images.

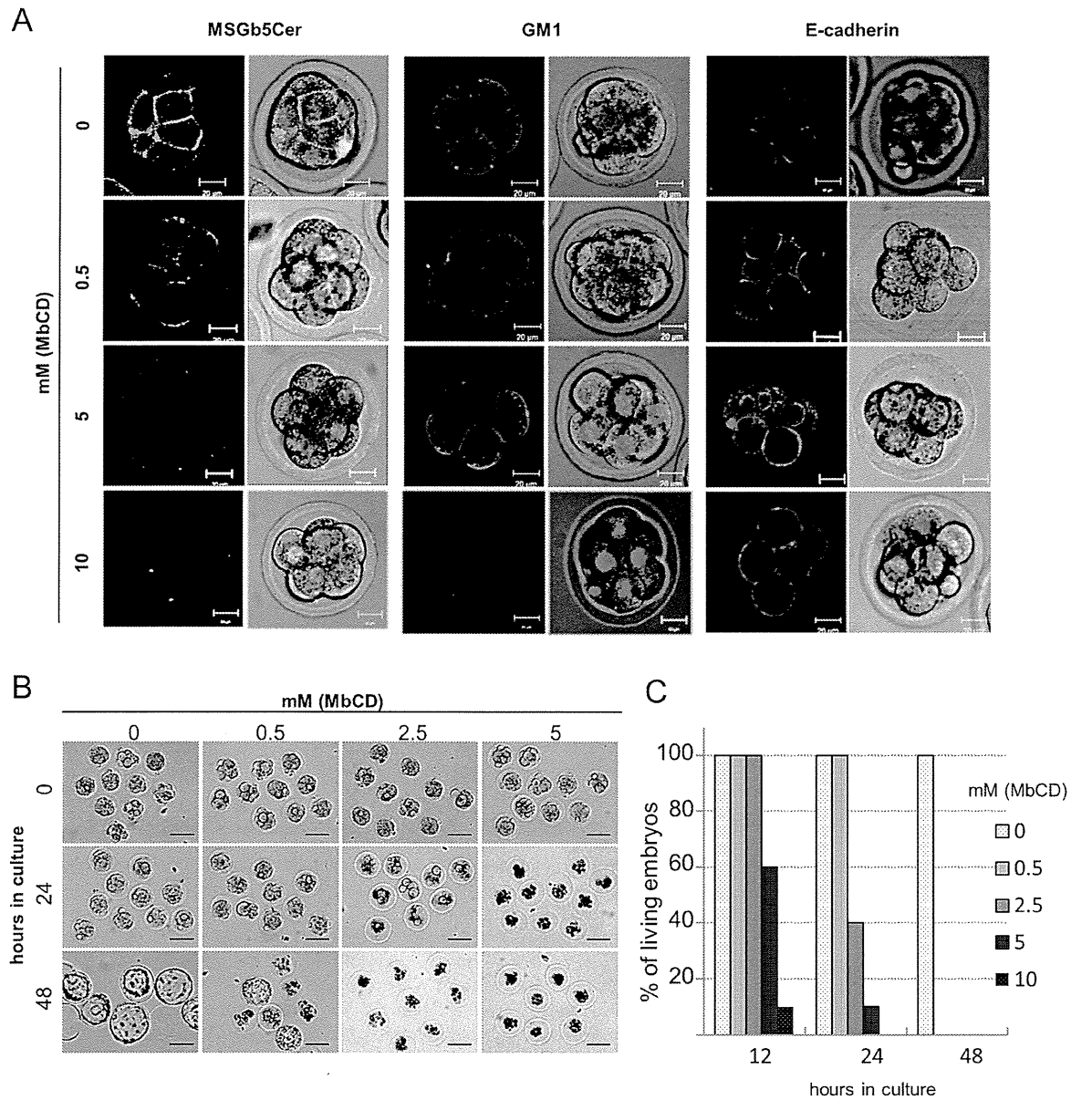

Figure 4 Pretreatment with MbCD inhibits cytokinesis and development of mouse preimplantation embryos. (A) Effect of MbCD on the expression of MSGb5Cer (green), GM1 (red) and E-cadherin (red) on 8-cell embryos. The left column and the right column of each panel represent a 2D image and the overlay of a 2D image and a differential interference contrast (DIC) micrograph, respectively. Thirty 8-cell embryos were used for the experiment represented in the images. (B) Representative DIC images of embryos cultured for 0, 24 and 48 hours in M16 medium after preincubation with 0-5 mM MbCD. Scale bars: 100 μm. Twenty 8-cell embryos were used for the experiment represented each images. (C) The percentages of living embryos cultured for 12, 24 and 48 hours after preincubation with 0-5 mM MbCD. Twenty 8-cell embryos were cultured for each concentration of MbCD.

In the 2-cell embryos cultured for 2 hours with 6E2, a large amount of F-actin accumulated at the interfaces, whereas no E-cadherin was detected at the interfaces, and it almost localized on the outer surface of blastomeres (Figure 5C). The entry of E-cadherin into the interfaces in living embryos was inhibited after treatment with Mab 6E2 in a dose-dependent manner (Figure 5D).

MSGb5Cer did not accumulate at the interfaces in actin-depolymerized 2-cell embryos

Actin filaments are thought to generate a mechanical force that drives membrane molecules or domains during cytokinesis. We investigated the effect of disruption of actin filaments with CCD on the localization of MSGb5Cer. As shown in Figure 6, when 2-cell stage embryos preincubated with 0, 0.2, and 2 μg/ml of CCD

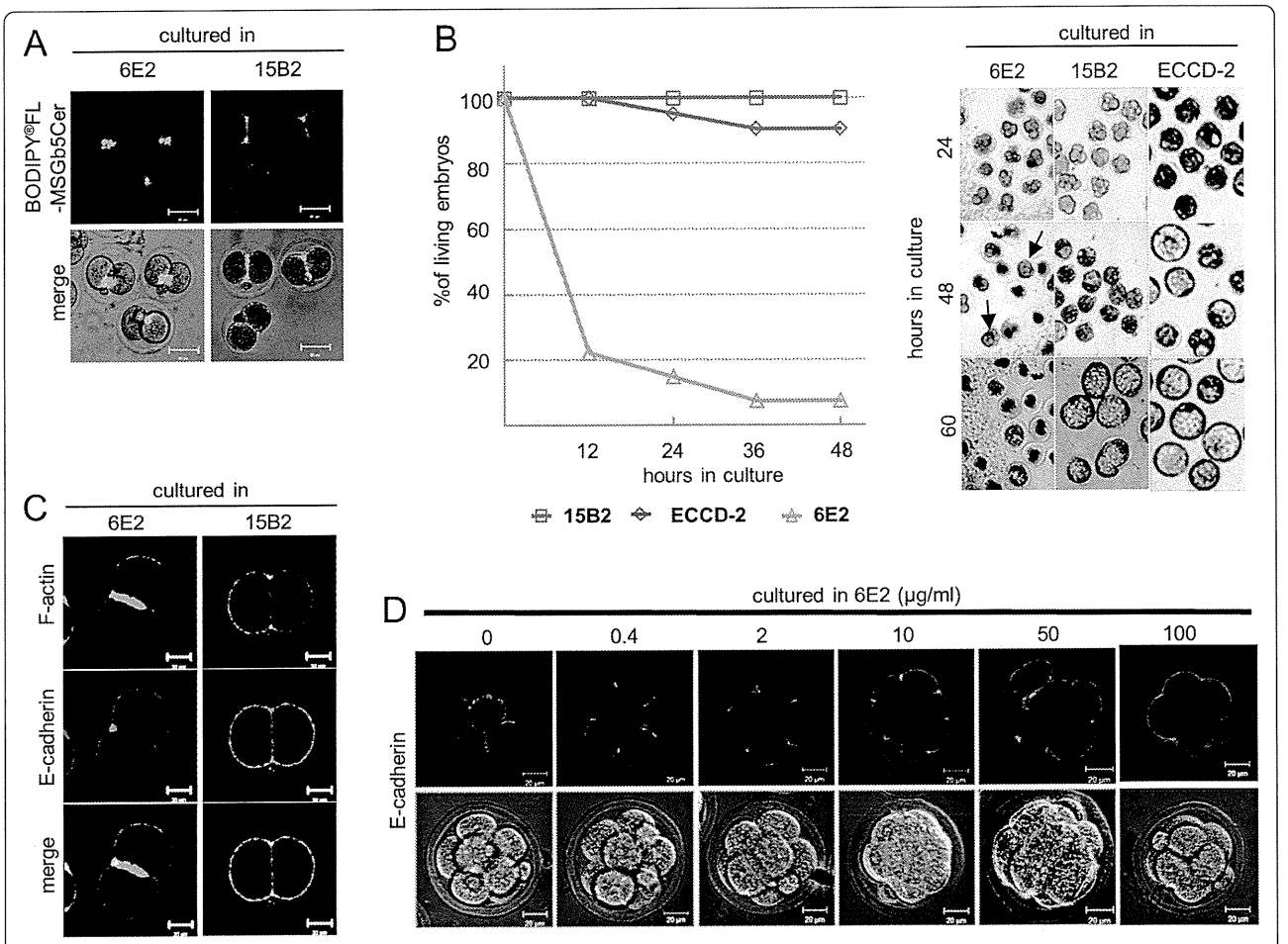

Figure 5 Extensive cross-linking of MSGb5Cer with 6E2 inhibits cytokinesis and development of mouse preimplantation embryos. (A) Deposition of BODIPY®FL-MSGb5Cer at the interfaces of 2-cell stage embryos cultured in the presence of 6E2. Embryos labeled with BODIPY®FL-MSGb5Cer (green) were cultured for 1 hour in M16 medium containing 100 μg/ml of 6E2 or 15B2 antibodies. A fluorescence 2D image of BODIPY®FL-MSGb5Cer and the overlay of a 2D image and DIC micrograph of cultured embryos are shown. These images shown are representative of twelve 2-cell embryos. (B) Effect of cross-linking of MSGb5Cer with 6E2 on cytokinesis and the development of mouse preimplantation embryos. Two-cell embryos were cultured for 60 hours in M16 medium containing 100 μg/ml of 15B2 (red squares), ECCD-2 (blue diamonds), and 6E2 (green triangles), and the living embryos were counted and their DIC images were taken at the times indicated. Arrows indicate compacted embryos. Twenty of 2-cell stage embryos were cultured for each experiment groups. (C) Localization of F-actin and E-cadherin in MSGb5Cer-cross-linked 2-cell embryos. Two-cell embryos treated for 2 hours with 6E2 (left column) or 15B2 (right column) were fixed and stained with Alexa Fluor® 633 phalloidin and anti E-cadherin/Alexa Fluor® 546-conjugated rabbit anti-rat IgG. These images shown are representative of twelve 2-cell embryos. (D) Inhibitory effect of cross-linking of MSGb5Cer with 6E2 on the localization of E-cadherin at interfaces. Embryos were immunostained with ECCD-2/Alexa Fluor® 546-conjugated Rabbit Anti-rat IgG (red) in the presence of various concentrations of 6E2. The upper row and the bottom row of each panel represent a 2D image and the overlay of a 2D image and DIC micrograph, respectively. These images shown are representative of thirty morula embryos.

were immunostained with anti-MSGb5Cer Mab 6E2, accumulation of MSGb5Cer at the interface was suppressed in a dose-dependent manner. These results suggest that inhibition of F-actin polymerization by CCD prevents the localization of MSGb5Cer at the interface.

Absence of E-cadherin causes heterotopic localization of MSGb5Cer on the blastomere surface

To investigate the involvement of E-cadherin in the localization of MSGb5Cer at the interface, we generated embryos lacking maternal E-cadherin, and examined them. In control 2-cell embryos (Genotype; Floxed/+), MSGb5Cer and E-cadherin exhibited a similar distribution pattern and accumulated at the interface (Figure 7 upper row). In E-cadherin null mutant 2-cell embryos (Genotype; Floxed del/+), adhesion between the blastomeres was weaker and the area of the interface plane was greatly reduced (Figure 7 middle and bottom row). In these embryos, MSGb5Cer formed heterotopic aggregates (indicated by the arrow) or assembled at the outer

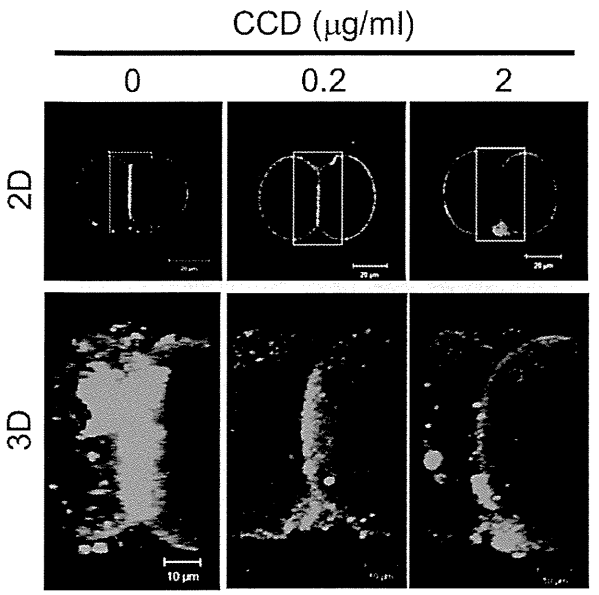

Figure 6 Disruption of actin filaments suppresses localization of MSGb5Cer at the interface. Two-cell embryos pretreated with 0, 0.2, and 2 μg/ml of CCD were immunostained with Alexa Fluor® 488-conjugated 6E2 (green). The 3D images were constructed by stacking optical slice images of the area enclosed by the square. Scale bar: 20 μm (2D), 10 μm (3D). These images shown are representative of thirty 2-cell stage embryos.

surface membranes of the blastomeres (indicated by the arrowhead). These results suggest that E-cadherin is required not for assembly, but for localization of MSGb5Cer at the interface of blastomeres.

Discussion and Conclusions

In this study, we investigated the involvement of MSGb5Cer in the development of mouse preimplantation embryos. As presented in Figure 2, MSGb5Cer moved to the future site of the cleavage furrow and accumulated at the interfaces between blastomeres as cytokinesis proceeds during embryonic development of mouse preimplantation embryos. Once, however, cytokinesis is complete the MSGb5Cer have accumulated at the interfaces evenly redistribute themselves over the cell surface (Figure 2).

MSGb5Cer is thought to be involved in the formation of raft membrane domains. Indeed, we observed overlapped localization of MSGb5Cer and cholesterol, an important constituent of lipid rafts (Figure 3). The finding that disruption of the integrity of lipid rafts by removal of cholesterol from the cell membrane with MbCD caused the release of MSGb5Cer into the perivitelline space (Figure 4) should further support above notion. Interestingly, as we presented in this study (Figure 1), GM1 and MSGb5Cer localize differently, suggesting that they may belong to different lipid rafts that possess distinct functions as described in several studies [16-18].

Since GM1 is easily detected with CTX-B, it is considered one of the most important marker GSLs for lipid rafts. Comiskey and Warner reported observation that GM1 visualized with biotinylated CTX-B were enriched at the cleavage furrow in mouse 2-cell and 4-cell embryos which actively undergo cytokinesis [10]. Burgess DR and his co-workers also reported that plasma membrane domains enriched in GM1 contain signalling machinery that contributes to cytokinesis and accumulate in the equatorial plasma membrane at mid-anaphase in sea urchin eggs [9], and further revealed that cells are polarized upon insertion of distinct basolateral membrane at the first division using the apical marker GM1 and the aPKC-PAR6 complex [19]. Although GM1 is constantly expressed throughout the cleavage stage in preimplantation embryos, MSGb5Cer is expressed only in the early cleavage stage from the unfertilized egg stage to morula stage embryos and more abundantly enriched at the cleavage furrow than GM1 during the course of cytokinesis (Figure 1). MSGb5Cer should therefore play a more specific role as a constituent of lipid rafts at this stage.

As described above, MbCD-mediated disruption of the integrity of lipid rafts caused the release of MSGb5Cer into the perivitelline space and decompaction of compacted 8-cell embryos and suppressed cell division. Comiskey and Warner also showed that cholesterol depletion by treatment of zygotes with MbCD inhibits preimplantation development from zygotes to blastocysts stage in culture in a dose-dependent manner [10]. On the other hand, heavy cross-linking of MSGb5Cer with MSGb5Cer-specific Mab induces extensive aggregation of MSGb5Cer (Figure 5) and suppressed cytokinesis. As a consequence, normal embryonic development would be terminated in both cases. Therefore, lipid rafts enriched in MSGb5Cer should play an important role in cytokinesis as well as in embryogenesis.

During cytokinesis, the cortical actin network form a scaffold for membrane proteins and thereby transfer them toward the cleavage furrow [3]. E-cadherin knockout mice display embryonic lethality and embryos are unable to form adhesion complexes [20,21]. In this study, we also presented close correlations between lipid rafts enriched in MSGb5Cer and E-cadherin as well as the cortical actin network. In preimplantation embryos, MSGb5Cer and E-cadherin are similarly distributed at the interfaces between blastomeres in 8-cell embryos, while MbCD-treatment caused the release of MSGb5Cer into the perivitelline space, decompaction of compacted embryos and even distribution of E-cadherin on the cell surface. In 2-cell embryos lacking E-cadherin, however, the MSGb5Cer-enriched lipid rafts accumulated